The Influence of Shear on Deep Convection Initiation. Part I: Theory

JOHN M. PETERS,[a] HUGH MORRISON,[b] T. CONNOR NELSON,[c] JAMES N. MARQUIS,[d] JAKE P. MULHOLLAND,[a] AND CHRISTOPHER J. NOWOTARSKI[e]

[a] Department of Meteorology, Naval Postgraduate School, Monterey, California
[b] National Center for Atmospheric Research, Boulder, Colorado
[c] Department of Atmospheric and Oceanic Sciences, University of Colorado Boulder, Boulder, Colorado
[d] Pacific Northwest National Laboratory, Richland, Washington
[e] Department of Atmospheric Science, Texas A&M University, College Station, Texas

(Manuscript received 24 May 2021, in final form 15 December 2021)

ABSTRACT: This article introduces a novel hypothesis for the role of vertical wind shear ("shear") in deep convection initiation (DCI). In this hypothesis, initial moist updrafts that exceed a width and shear threshold will "root" within a progressively deeper steering current with time, increase their low-level cloud-relative flow and inflow, widen, and subsequently reduce their susceptibility to entrainment-driven dilution, evolving toward a quasi-steady self-sustaining state. In contrast, initial updrafts that do not exceed the aforementioned thresholds experience suppressed growth by shear-induced downward pressure gradient accelerations, will not root in a deep-enough steering current to increase their inflow, will narrow with time, and will succumb to entrainment-driven dilution. In the latter case, an externally driven lifting mechanism is required to sustain deep convection, and deep convection will not persist in the absence of such lifting mechanism. A theoretical model is developed from the equations of motion to further explore this hypothesis. The model indicates that shear generally suppresses DCI, raising the initial subcloud updraft width that is necessary for it to occur. However, there is a pronounced bifurcation in updraft growth in the model after the onset of convection. Sufficiently wide initial updrafts grow and eventually achieve a steady state. In contrast, insufficiently wide initial updrafts shrink with time and eventually decay completely without external support. A sharp initial updraft radius threshold discriminates between these two outcomes. Thus, consistent with our hypothesis and observations, shear inhibits DCI in some situations, but facilitates it in others.

KEYWORDS: Convective clouds; Cumulus clouds; Storm environments; Supercells; Conservation of mass; Convective storms

1. Introduction

The onset of cumulonimbus convection is colloquially referred to as deep convection initiation (DCI). A comprehensive understanding of DCI in research and forecasting remains elusive. Global forecast and climate models that use convective parameterizations (CPs) struggle with their predictions of the timing of DCI (Dai et al. 1999; Yang and Slingo 2001; Betchold et al. 2004; Collier and Bowman 2004; Dai 2006; Covey et al. 2016; Christopoulos and Schneider 2021), often depicting an erroneously early onset of convective precipitation over land relative to observations. Many studies have directly addressed this problem over the past several decades through analysis of large-eddy simulations and targeted observations. A variety of themes have emerged from these studies:

- The elimination of convective inhibition (CIN) does not guarantee DCI (Derbyshire et al. 2004; Houston and Niyogi 2007; Nelson et al. 2021). For a cumulus cloud to grow deep, the low-level updraft must be sufficiently wide, and the environmental relative humidity (RH) must be sufficiently large, for the updraft to overcome the negative effects of entrainment (Turner and Taylor 1957; Turner 1964; Simpson and Wiggert 1969; McCarthy 1974; Kain and Fritsch 1990; Khairoutdinov and Randall 2006; Morrison 2017; Morrison et al. 2020; Peters et al. 2020a; Morrison et al. 2022).
- Ascent related to fronts, drylines, outflow boundaries, terrain-induced circulations, and other mesoscale flow features moistens the lower troposphere, widens clouds, and thus facilitates DCI (Kuang and Bretherton 2006; Khairoutdinov and Randall 2006; Schlemmer and Hohenegger 2014; Torri et al. 2015; Rousseau et al. 2017; Kurowski et al. 2018; Nelson et al. 2021; Marquis et al. 2021).
- DCI may be facilitated by ill-fated precursor updrafts that terminate their ascent at low altitudes, which moisten the lower atmosphere via detrainment of cloudy air and promote subsequent thermals to ascend to greater heights (Damiani et al. 2008; Waite and Khouider 2010; Moser and Lasher-Trapp 2017).

The aforementioned studies have primarily focused on thermodynamic, rather than kinematic, factors influencing DCI. What has been less studied is the influence of vertical wind shear (hereafter "shear") on DCI. Furthermore, there is little consensus on whether shear should influence DCI in a positive or negative way. For instance, there is scattered evidence in past literature that shear may hinder DCI. Simulations in Markowski and Richardson (2010) showed that unsheared dry updrafts grow deeper than their Peters et al. (2019a) showed similar results, with moist updrafts in sheared flow generally having shallower terminus heights than

Corresponding author: John M. Peters, jmpeters@nps.edu

DOI: 10.1175/JAS-D-21-0145.1

sheared counterparts. These authors attributed the aforementioned difference to larger entrainment-driven dilution of plume buoyancy in sheared environments than in unsheared environments. A study of simulated moist updrafts by moist updrafts in unsheared flow (also see Grabowski and Clark 1993; Kirshbaum and Straub 2019). However, these differences in moist updrafts largely arose from stronger downward-oriented pressure gradient accelerations acting upon moist updrafts in sheared environments than in unsheared environments. Indeed, simulations of terrain-induced DCI by Nelson et al. (2022) suggest that DCI is more inhibited when shear is strong, compared to when shear is weak. Overall, these studies suggest that shear may inhibit DCI by slowing or preventing the transition from shallow to deep convection, and we call this potential negative influence of shear on DCI the "shear suppression effect."

There are, however, potential pathways for shear to positively influence DCI. For instance, shear results in wider mature supercell (Warren et al. 2017; Trapp et al. 2017; Marion and Trapp 2019; Peters et al. 2019b, 2020d) and squall line (Mulholland et al. 2021) updrafts than in weakly sheared environments. These wide updrafts in strongly sheared environments are less susceptible to entrainment-driven dilution, and hence are deeper and have faster vertical velocities (hereafter w) than their weakly sheared counterparts (Peters et al. 2019b, 2020c). Marion and Trapp (2019) argued that shear should cause initially narrow and shallow updrafts to widen and deepen from their onset. These authors showed that updrafts in shear create a low-level dynamic low pressure "footprint" (Rotunno and Klemp 1982; Klemp 1987) with a larger horizontal expanse than the updraft itself. Because this pressure "footprint" is wider than the updraft, upward-oriented dynamic pressure accelerations will tend to lift low-level parcels to their levels of free convection (LFC) over a wider region than the updraft itself, expanding the updraft with time. This process leads to a gradual widening, and consequently deepening, of initially narrow and shallow updrafts into a supercell. However, initially narrow and shallow updrafts do not always grow into supercells in strongly sheared environments. In fact, the physical processes differentiating updrafts that widen and deepen within ambient shear from those that do not are left unexplained by all of the studies summarized above.

The knowledge gaps described thus far lead to the following question, which motivates our study: Under what conditions does shear aid or inhibit DCI? We begin with a proposed answer to this question, which we term the "progressive rooting hypothesis." In this hypothesis, under certain conditions, shear will cause initial updrafts to widen and deepen until they reach a steady state. This deepening is caused by sheared updrafts rooting within a steering current that is sufficiently fast to increase their low-level cloud-relative inflow, and subsequently, their width (Peters et al. 2019b). For progressive rooting to occur, an updraft must widen and deepen at a sufficiently fast rate to overcome the deleterious effects entrainment-driven dilution and the shear suppression of cloud ascent rates. In situations where the aforementioned process does not occur, DCI is generally suppressed via the shear suppression effect.

We address the progressive rooting hypothesis using a combined theoretical and numerical modeling approach. In the present study (Part I), we develop a theoretical model from the governing equations of the atmosphere that embodies key elements of the progressive rooting hypothesis. We use this theoretical model to elaborate on the hypothesis by demonstrating the model's behavior across a large environmental parameter space.

This exercise will help us specify under what conditions shear will "help or hurt" DCI. In Peters et al. (2022b, hereafter Part II), the behavior of the theoretical model is evaluated against a large number of numerical simulations. In that study, we first determine whether the numerical simulations behave in a way that is consistent with the theoretical model. We then scrutinize key assumptions of the theoretical model via a detailed investigation of dynamics in the simulations. Thus, the progressive rooting hypothesis is introduced and elaborated upon in Part I, and evaluated with simulations in Part II.

The paper organization is as follows: A theoretical model for DCI is developed in section 2. In section 3, we use this theoretical model to explore the shear suppression effect and progressive rooting hypothesis in a large parameter space of thermodynamic and wind environments, and section 4 summarizes our conclusions.

2. Conceptual overview of the theoretical model

The general framework for our theoretical model originate from Morrison et al. (2022), who showed that the depth of an unsheared convective updraft is intrinsically dependent on the width of the region of ascent below the LFC that "triggers" the cloud (hereafter the sub-LFC updraft), the environmental RH above the LFC,[1] and the buoyancy B of an undiluted parcel (B_{UD}) above the LFC. When all three of these factors are large, the entrainment-driven dilution is small and updrafts grow deep, resulting in DCI. In contrast, when certain combinations of the three of these factors are small, entrainment-driven dilution is large and ascending air within clouds becomes negatively buoyant in the lower troposphere, preventing DCI. We build upon this existing concept by exploring the added influence of shear.

The parameters that are input into our theoretical model are an initial subcloud updraft radius R_0, RH, B_{UD}, and shear magnitude s. We assume that early cloud evolution consists of discrete rising thermal-like cloud elements. The vertical space between these thermals will consist of weak or even vanishing updraft in the case of narrow initial thermals, or somewhat continuous updraft in the case of wide initial thermals (as was shown in Morrison et al. 2020; Peters et al. 2020a). Each thermal rises over time scale Dt and has a termination height H, which is defined as the height where the thermal ascent rate W vanishes. The variable H serves as a direct metric for cloud depth, and will be used to assess whether or not DCI has occurred. The parameter W, and consequently H, are

[1] Entrainment below the LFC and above the lifted condensation level is neglected for simplicity.

modulated in our model by B and vertical perturbation pressure gradient accelerations (PAs). The fractional entrainment rate «, the magnitude of which is inversely proportional to cloud radius R (Morton et al. 1956; McCarthy 1974; Scorer 1957; Turner 1964; Simpson and Wiggert 1969; Kain and Fritsch 1990; Khairoutdinov and Randall 2006; Kirshbaum and Grant 2012; Hernandez-Deckers and Sherwood 2018), constrains updraft evolution by diluting B, and thus modulates W and H.

Note that for environments with large RH and sufficiently large R_0, theory and idealized simulations suggest that initial updrafts may behave more like a single or series of startingplumes (Turner 1962) with a thermal-like leading edge and a continuous plume-like updraft region that trails the leading edge, than like a chain of discrete thermals (Morrison et al. 2020; Peters et al. 2020a). Certain aspects of our theoretical model will account for this behavior, as is detailed in the next subsection. For ease of description we will refer to all rising cloud elements as "thermals," with the understanding this includes both discrete rising cloud bubbles (traditionally considered as cloud "thermals") as well as rising plume-like features.

To encapsulate the progressive rooting hypothesis, our model must characterize how the time-dependent updraft radius R evolves. For the initial thermal that rises above the LFC, we assume that $R = R_0$. That is, the width of this thermal is equal to the width of the region of initial sub-LFC ascent. For simplicity, we will assume that there is a discrete pulse of externally driven sub-LFC updraft that triggers the cloud, and that this finite pulse ceases once the first moist thermal begins to rise. This is akin to assuming that clouds are triggered by eddies in the planetary boundary layer (PBL), which exist over relatively short time scales.

In positively buoyant convection, negative buoyancy pressure perturbations reside near updraft base with a magnitude that scales with the updraft B and a characteristic width that scales with, and is often wider than, the width of the updraft (Doswell and Markowski 2004; Morrison 2016). Likewise, when shear is present, negative dynamic pressure perturbations are typically present near updraft base, with magnitudes that scale with velocity gradients in the updraft, and a characteristic width that also scales with, and is often slightly larger than, the width of the updraft (Rotunno and Klemp 1982; Davies-Jones 2002; Marion and Trapp 2019). We assume that these negative pressure perturbations result in persistent upward accelerations below the LFC that drive continued moist convection after the initial "pulse" from a PBL eddy. This assumption is supported by extensive analyses of trajectories in numerical simulations in section 5 of Part II. Because these pressure perturbations are typically more expansive than the updraft itself, they will generally drive updraft expansion with time (as was described in Marion and Trapp 2019). However, because these pressure perturbations are also intrinsically connected to the characteristics of the overlying updraft, processes such as entrainment or decreasing inflow with time that cause updraft B, w, and R to decrease may counteract this pressure-driven tendency for widening in certain situations, leading to a narrowing and decaying cloud.

The first thermal rises over time scale Dt_1 to height H_1. At this point the ambient wind will begin to advect the cloud downstream, establishing a cloud motion vector. In the presence of shear, the low-level cloud-relative flow is altered by this change in cloud motion, changing the cloud's low-level inflow. From mass continuity, the changing inflow results in a change in vertical mass flux related to the next thermal. Because w is strongly modulated by B (Peters 2016; Jeevanjee 2017; Morrison and Peters 2018; Peters et al. 2020b), this change in vertical mass flux primarily manifests in the radius R_1 of the next thermal (or starting plume) in the "lineup" being different than R_0 (Peters et al. 2019b). This new thermal rises over time scale Dt_2 to height H_2, which may be different from H_1. Consequently, the cloud once again alters its motion and its inflow, leading to the development of a new thermal with radius R_2. This process then continues until the cloud either reaches a steady state, or decays completely.

If s and H_1 are sufficiently large, the cloud will increase its inflow quickly enough to result in $R_1 . R_0$. Because s in this situation is large, the first thermal will experience a substantial downward oriented dynamic PA (DPA) from the shear suppression effect (Peters et al. 2019a). However, because $R_1 . R_0$, the second thermal may reach a greater termination height H_2 than the first thermal's termination height H_1, and in that case would establish a faster cloud motion because it taps into stronger flow aloft in the presence of shear. The second thermal will also experience a weaker DPA associated with the shear suppression effect since the magnitude of this effect is inversely proportional to R [this dependency of the shear suppression effect on R is described in Peters et al. (2019a)]. Because of the faster motion, the low-level cloud-relative inflow will also increase, leading to a new wider radius $R_2 . R_1$ for the next thermal in the "lineup." This process continues until the cloud has achieved steady H and R. We refer to the updrafts that develop via this process as "steady, self-sustaining," because they may continue to exist on their own volition indefinitely with or without an external factor that continues to create new sub-LFC updrafts.

If the cloud-relative flow and inflow corresponding to H_1 are not sufficiently large to make $R_1 . R_0$, subsequent moist thermals will be generated by progressively narrower regions of sub-LFC ascent, have correspondingly decreased R, and will consequently ascend to lower heights than the first thermal. Thus, the cloud will eventually dissipate in the absence of a persistent externally driven sub-LFC updraft. This is not to say that all clouds for which R_1 , R_0 do not develop sustained deep convection. Rather, for sustained deep convection to occur in the R_1 , R_0 scenario, an external factor such as an air mass boundary or terrain feature must continuously generate new sub-LFC updrafts. We refer to deep convection in this situation as "externally modulated," because of this requirement for a persistent externally driven sub-LFC updraft to maintain deep convection.

3. Quantitative description of the theoretical model

This section provides a detailed mathematical description of our theoretical model. A list of symbol definitions is provided in Table

1, and critical assumptions and their justifications are listed in Table 2.

a. Determining H of the initial rising thermal

Given a vertical environmental profile, which provides B_{UD}, RH, and s, we must develop an equation that determines H for a thermal that is rising with a given R. We begin

TABLE 1. List of acronym, variable, and symbol definitions.

Acronym, variable, or symbol	Mathematical definition	Description in words
DCI		Deep convection initiation
RH		Relative humidity
B	Eq. (27)	Buoyancy
B_{UD}		Buoyancy for an undiluted parcel lifted from the height of maximum moist static energy
W		Ascent rate of thermal
H		Termination height of thermal
Dt		Time it takes thermal to ascend from LFC to H
R_0		Radius of initial sub-LFC updraft and starting radius of cloud
PA	$2\frac{1}{\rho_0}\frac{\partial p}{\partial z}$	Vertical pressure gradient acceleration
«	Eq. (7)	Fractional entrainment rate
s	$\frac{du^0}{dz}$	Ambient shear in a cloud's environment
p_B	$\int p_B \partial z$	Buoyancy pressure
p_D	$\zeta^2 p_D$ $2\zeta \cdot r_0(V \cdot \zeta)V$	Dynamic pressure
BPA	$2\frac{1}{\rho_0}\frac{\partial p_B}{\partial z}$	Buoyancy pressure acceleration
	$-\frac{1}{\rho_0}\frac{\partial p_D}{\partial z}$	DPA $2\frac{1}{\rho_0}\frac{\partial p_D}{\partial z}$ Dynamic pressure acceleration
f		Volume average of arbitrary scalar f within thermal
f_0		Height dependent reference profile of arbitrary scalar f
w_c	Eq. (12)	w at thermal center
w_b	Eq. (17) w	w at thermal bottom $\equiv \lvert \lvert \frac{\lvert}{W}$
B_m	Eq. (5)	Maximum B within thermal
$\overline{f}^a$	$a \equiv \frac{\overline{w}}{}$	Horizontal average of arbitrary scalar f within thermal
L_B	w_c	Depth over which $B_m > 0$

c_{pd}		Specific heat of dry air at constant pressure
$L_{y,ref}$		Reference latent heat of vaporization at 273.15 K
q_s		Saturation vapor pressure over liquid
k		Mixing constant
P_r		Turbulent Prandtl number
L	L = R/3	Horizontal mixing length
j		Dynamic entrainment factor
V	Eq. (6)	Term in B_m equation accounting for entrainment of dry air
Du		Difference in u between top and bottom of toroidal circulation
f^		Vertical and azimuthal average of arbitrary variable f
U		Departure of thermal's u wind speed from u_0
u_r		Radial wind in cylindrical coordinates
w_{top}		Radially dependent profile of w at thermal top
w_{cent}		Radially dependent profile of w at vertical center of thermal
w_{bot}		Radially dependent profile of w at thermal bottom
$u_{rbot-cent}$ $u_{rcent-top}$		Azimuthal and vertical average of u_r from thermal center to top
c_z		Azimuthal and vertical average of u_r from thermal bottom to center
c_x		Thermal drag coefficient in vertical direction
	Eq. (18)	Thermal drag coefficient in horizontal direction
w_{max}		Maximum in w_c as a thermal ascends from the LFC to H
s		Ratio of height of w_{max} to H
V_{CR}		Cloud-relative flow
#		Fraction of V_{CR} that turns upward into updraft
z_{wc}		Maximum height of w_c . 0
z_{wb}		Maximum height of w_b . 0
MSE	Eq. (24)	Moist static energy
q_y		Water vapor mass fraction
q_t		Total water mass fraction
R_y		Specific gas constant for water vapor
R_d		Specific gas constant for dry air
u		Potential temperature

TABLE 2. List of critical theoretical assumptions and their justifications.

Assumption	Justification (if any)
Momentum entrainment neglected in Eq. (1)	Supported by previous studies (e.g., Sherwood et al. 2013)
$W = lw_c$ in Eq. (4), where $l \approx 0.5$	Supported by previous studies (e.g., Romps and Charn 2015)
1	

$\frac{I^2}{W} B \approx B_m$ in Eqs. (3) and (4) Supported by previous studies (e.g., Morrison 2017) aw_c in Eq. (4) Supported by previous studies (e.g., Morrison and Peters 2018)

u_{rc2t} a max(u) (u) in Eq. (12)
$u_{r\ t})2$ max(u_r
0:2 1 2 $\frac{w}{w_c}$)

Height of w_{max} is sH_i in Eq. (19), where s is constant Supported by Peters et al. (2020b)
Inflow is entirely determined by V_{CR} in Eq. (20) Supported by analyses of numerical simulations in section 4 of Part II
Inflow is composed of air both within and above the EIL Supported by past research (Schiro et al. 2018; Nowotarski et al. 2020)
All V_{CR} turns entirely upward once it crosses the updraft periphery Supported by analyses of numerical simulations in section 4 of Part II
Advective cloud motion is characterized by the average flow within the depth of continuous updraft in Eq. (23)
Lateral mixing at a given level occurs linearly in Eqs. (28)

u_{rb2c} a u_r (12) Du max
$_b$ in Eq. (12)

c_z b in Eq. (18) Supported by Peters et al. (2019a)

and (29)

with an approximate equation for the Lagrangian tendency for W following the thermal:

$$\frac{dW}{dt} B \overline{2 r\tilde{1} \partial p_{ZB}} \overline{2 r\tilde{1} \partial p_{ZD}}, \quad (1)$$

where the angle brackets denotes a volume average within the thermal, B is buoyancy, $\overline{2\ 1=r\partial p_B=\partial z}$ represents buoy- ancy pressure acceleration (BPA), and $\overline{2\ 1=^r\partial p_D=\partial z}$ represents DPA. We have neglected the momentum entrainment terms that would show up in the precise form of this equation because previous authors have shown that the contributions of the neglected terms to W are often an order of magnitude smaller than those retained (Sherwood et al. 2013; Romps and Charn 2015; Hernandez-Deckers and Sherwood 2016; Morrison and Peters 2018).

It will become useful for later derivations to define w at specific locations within the thermal, in addition to characterizing the thermal's ascent rate W. For instance, w_t, w_c, and w_b, are defined as w at the thermal top, center, and bottom, respectively, along the thermal's central vertical axis at r = 0. For simplicity, we assume that the spacing between each of these w locations is R, the thermal's radius. By definition, $w_t = W$, since the thermal's top must rise at a rate equal to the ascent rate of the thermal as a whole. We also assume that w_c is proportional to W, such that $w_c = l^{21}W$, where $0 \# l\# 1$ is a parameter that is set to 0.5 here based on results from Romps and Charn (2015) and Morrison and Peters (2018). Figure 1 provides a visual guide for where each of these quantities is located within a cloud, and relative to a rising thermal.

We note that $dW=dt\ \ dW=dz dz=dt\ \ 1=2dW^2{}_2=dz_1$, where d=dz is the change in a quantity with the change in a thermal's vertical position. We also substitute $w_c = l\,W$, giving

$$\frac{dw^2_c}{dz} \frac{2}{l_2} \frac{2}{B} \frac{1}{2l_2 r} \frac{\partial p_B}{\partial z} \frac{2_2 1}{2l r} \frac{\partial p_D}{\partial z}: \quad (2)$$

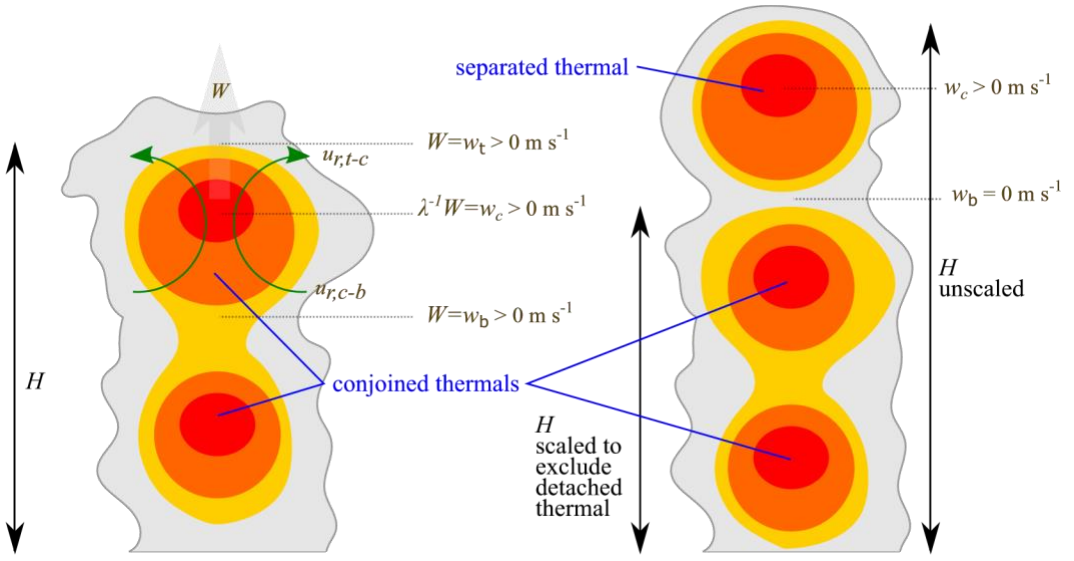

FIG. 1. Schematic illustrating various aspects of assumed updraft structure in the theoretical model. Yellow, orange, and red shading indicate weak, moderate, and strong upward w, respectively. (left) A cloud is composed of two thermals embedded with a continuous region of ascent (i.e., w_b . 0 m s^{21}). In this case, H is set to the entire cloud depth. (right) A cloud is composed of three thermals. The two lower thermals are embedded within a continuous region of ascent, whereas the top thermal is separated from the bottom two thermals by a region where no ascent is occurring (i.e., w_b = 0 m s^{21} for the top thermal). In this case, H is rescaled to the depth of the updraft encompassed

We assume that the magnitude of w_c is well described by accelerations from B and BPA at the location within the thermal of the maximum B, which usually resides near updraft top for ascending updraft below the sounding's level of neutral buoyancy, following results of Peters (2016). We also assume that the thermal as a whole experiences dynamic pressure drag based on results from Morrison and Peters (2018). These assumptions imply that

$$1=l^2\ B \approx B_m \text{ and } 2\quad 1=\frac{l}{2}\quad 1=\frac{r\partial p_B}{\partial z}\approx 21=\frac{r\partial p_B}{\partial z_m},$$

where the subscript m indicates the value at the location of maximum B.

The following analytic approximation for $21=\frac{r\partial p_B}{\partial z_m}$ was derived in Morrison (2016):

$$2-\frac{1}{R}\frac{\partial p_B}{B}\approx 2\ 1\ 1\ \frac{L_B^2}{2\ 2}\ ^{21}\ m\ B\ ,\quad (3)\ r\partial z_m\ 2a$$

where L_B is the depth over which B_m is positive in the updraft, 0 ,a# 1 is a constant defined such that w_c aw_c, and w_c is the horizontal average of w at the vertical thermal center. This expression accounts for the fact that BPA becomes increasingly large and downward oriented as updrafts become wider, and vanishes for increasingly narrow updrafts. Combining these expressions for B and BPA gives

$$\frac{dw_c^2}{dz}\quad 2\ 1\ 1\ L\quad \frac{2a^2{}_{2B}R^{221}}{B}\ m\ \frac{2_2\ 1\ \partial p_D}{2l\ r\partial z}\ :\qquad (4)$$

The following analytic approximation for B_m as a function of z and R was derived in Morrison et al. (2020):

by the lower two connected thermals.

$$B_m(z, R)\ \frac{B_{UD}(\ )z\ 2\alpha z\alpha V(\ )z\ ,}{11\ \frac{}{2}}\qquad (5)$$

$$V(\ )z \equiv \frac{2L\quad g\quad z\,z}{y,ref}\ \int^{z^*}\ \frac{}{q_{s,0}(1\ 2\ RH^{\ })}\,dz^*,\qquad (6)$$

$$\frac{c_{pd}\quad z\,0\,T_0\,11\,L_{y2,ref}q_{s,20}\,c_{pd}R_y}{2jLk^2}\ T_0\ «\equiv\ \frac{}{P_rR_2}\ ,\qquad (7)$$

where B_{UD} is valid for a parcel lifted from the height of maximum moist static energy (MSE), $L_{y,ref}$ is a constant reference latent heat

of vaporization, « is a fractional entrainment rate, g is the gravitational constant, c_{pd} is the specific heat of dry air at constant pressure, $q_{s,0}$ is the saturation mixing ratio of the background environment, R_v is the specific gas constant for water vapor, T_0 is the temperature of the background environment, k is a mixing constant, P_r is the turbulent Prandtl number, L is a turbulent mixing rate that is set to R=3 to remain consistent with Peters et al. (2020a), and j$ 1 is a parameter that accounts for dynamic entrainment (Morrison et al. 2020; Peters et al. 2020a). Because dynamic entrainment is typically maximized near the base of a thermal and minimized near the thermal center and top owing to the thermal's toroidal circulation (Morrison et al. 2020), j= 1 at the height of B_m. The «V term accounts for the influence of the entrainment of dry air on B_m, and the «z=2 term accounts for the direct dilution of B_m via the entrainment of nonbuoyant air from an updraft's surroundings. Combining these expressions with Eq. (4) gives

$$\frac{dw_{c2}}{dz} \quad 2\,11\ 2a\,22BR2 \quad BUD(\,)z\ 2k2R\ V(\,)z\ 2l22\,r1\ pzD: \qquad (8)$$

The remaining unknown in this equation is the $1=\rho_D=z$ term. Although recent work has shown that this acceleration has little effect on rising dry buoyant thermals (Morrison et al. 2021, manuscript submitted to J. Atmos. Sci.), dynamic pressure accelerations in rising moist thermals generally acts in opposition to B (Morrison and Peters 2018). Thus, following other simplified models for moist thermals' ascent (e.g., Romps and Kuang 2010b; Romps 2016), we parameterize this unsheared component as $3c_z=8RW^2$ $3c_z=8Rl^2w^2_c$, which is the standard drag law formula for a sphere, where c_z is a vertical drag coefficient that will be discussed later. An additional drag occurs when the thermal rises through a sheared environment. The scaling for this shear-induced drag $21=\rho_D=z \sim DuU=R$ was derived in Peters et al. (2019a), where Du is the vertical wind difference between the top and bottom of a thermal's toroidal circulation, U is the thermal's x, or zonal, velocity, and U = U 1 u_0, where U is the departure of the thermal's u wind speed from the background profile $u_0(z)$. This relation is assumed to scale with the drag coef$_z$ficient c_z, so we write $21=\rho_D=z \sim c\,DuU=R$ for the shear-induced part of the drag.

The quantity Du may be represented in terms of known quantities by making use of the azimuthally averaged cylindrical continuity equation, which is written as

$$1\ \frac{(u_r r)}{r}\ w \quad r \quad z \quad 1 \quad 0, \qquad (9)$$

where u_r is the radial wind, a tilde (˜) represents the azimuthal average, and r is the radial coordinate. Integrating this equation from the thermal center to the thermal top (a distance of R), and from r = 0 to r = R, gives $u_{rcent\text{-}top}\ 1\ w_{top}\ 2\ w_{cent}\ 0$, (10)

where w_{top} and w_{cent} are the radially dependent profiles of w at the top and center of the thermal, respectively. Likewise, integrating over the volume of a cylinder from the thermal bottom to its center and r = 0 to r = R gives

$$u_{rbot\text{-}cent}\ 1\ (w_{cent}\ 2\ w_{bot})\ 0, \qquad (11)$$

where w_{bot} is the radially dependent profile of w at the bottom of the thermal. Figure 1 once again provides a visual guide for where in individual thermals described quantities are evaluated. Recall that u is radial wind, $_{cent\text{-}top}$ and $_{bot\text{-}cent}$ denote vertical averages at R_r from the center to the top, and the bottom to the center, respectively, of the thermal, and the overbar denotes a horizontal area average within R at a fixed height. Next, we assume that averages over a certain height range for u or horizontal area range for w are proportional to the maximum values over these ranges via the constant proportionality factor a.

These assumptions imply $u_{rcent\text{-}top}$ $a\,max(u_r)_{top}$, $u_{rbot\text{-}cent}$ $a\,max(u_r)_{bot}$, Du $max(u_r)_{top}\ 2\ max(u_r)_{bot}$, w_{cent} aw_c, w_{top} aw_t aW alw_c, and for a coherent thermal w_{bot} w_{top}, where $max(\,)_{top}$ and $max(\,)_{bot}$ are the maxima over the middleto-top and bottom-to-middle height ranges, respectively.

Combining Eqs. (10), (11), (1), and the aforementioned assumptions gives

$$\frac{dw}{dz} = \frac{2}{1+2a}\left[\frac{L_{2B}^2}{R^2}\left(\frac{1}{1+2a}\right)B_{UD}(z) - \frac{1}{2}k^2 R k z^2 V(z)\right] - \frac{1}{R}\left(\frac{1}{1+2a}\right)w_c U - \frac{1}{3}w_c^2. \quad (12)$$

Note that from Eq. (12), we may calculate the time Δt that it takes a thermal to ascend from the LFC to H as

$$\Delta t = \int_{z_{LFC}}^{z_H} \frac{1}{w_c}\,dz.$$

To obtain an expression for the thermal's local departure from the background wind U, we introduce an approximate equation for the thermal's horizontal velocity in the x, or zonal, direction U, which is given as

$$\frac{dU}{dz} = \frac{1}{\rho}\frac{dp}{dx}, \quad (13)$$

where $p = p_B + p_D$. We assume that a thermal only encounters shear in the x, or zonal, direction and therefore omit an analogous equation for V, the thermal's velocity in the y direction. By noting that $U = U + u_0$, and by using the chain rule $dU/dt = w\,dU/dz$, where dU/dz is the change in U at the location of the thermal as the thermal changes height, we may rewrite Eq. (13) as

$$\frac{dU}{dz} = \frac{1}{w_c}\frac{dU}{dx} = \frac{1}{\rho}\frac{dp}{dz}. \quad (14)$$

We again parameterize $1/\rho\,dp/dx$ using standard drag law formula for a sphere, giving

$$\frac{1}{\rho}\frac{dp}{dx} \approx \frac{3c_x}{8R}U^2, \quad (15)$$

where $c_x = 0.2$ is the horizontal drag coefficient, set to that for a solid sphere in high Reynolds number flow for simplicity, similar to Romps and Kuang (2010a). In combining Eq. (14) with Eq. (15) and noting that the shear s may be defined as $s = du_0/dz$, we obtain

$$\frac{dU}{dz} = \frac{1}{w_c}\frac{3c_x}{8R}U^2 + s. \quad (16)$$

The remaining undefined parameter is c_z. The shear suppression effect specifically pertains to rising moist thermals that have well-defined toroidal circulations. For moist updrafts that behave like a continuous plume, however, the shear suppression effect should become less influential. To represent this transition from strong shear suppression when updrafts are thermal-like, to vanishing shear suppression when updrafts are plume-like, we must develop an objective metric to define the degree to which an updraft behaves like thermals or plumes. To accomplish this we introduce an equation for w_b, which is the w near the thermal bottom, similar to Eq. (12) for w_c:

$$\frac{dw_b^2}{dz} = \frac{2}{1+\frac{2a^2R^2}{L_B^2}}\frac{B_{UD}(z-R) - \frac{9k^2}{2R}V(z-R)}{1+\frac{9k^2}{4R}(z-R)} - \frac{2}{R}\frac{z}{c}\frac{2(1-\rho)}{\rho^2}w_c U - \frac{3}{4}w_c^2. \quad (17)$$

Note that we have assumed that the thermal as a whole experiences the same downward dynamic pressure drag, and thus the dynamic pressure acceleration term is the same as Eq. (12). However, we have made the following adjustments relative to Eq. (12): B_{UD} and V are evaluated at z–R instead of z, to reflect that w_b is valid at thermal bottom, which is distance R below w_c, and both of the entrainment related terms (i.e., those containing k^2) have been multiplied by 9/4. This multiplicative factor follows from the theoretical analyses of Morrison (2017) and Morrison et al. (2020) to represent the effects of enhanced lateral entrainment at the thermal base driven by the inward branch of the thermal's toroidal circulation (i.e., dynamic entrainment).

Because of this multiplicative factor, w_b, w_c for all heights below the height of maximum B_m. When $w_b = 0$ the updraft behaves like an isolated thermal because its w is vertically discontinuous. In contrast, $w_b \approx w_c$ indicates that an updraft is plumelike or starting-plume-like, because given local updraft w maxima are continuously connected to updraft regions above and below. To capture this behavior and give $c_z \approx 0$ for plume-like updrafts and $c_z \approx 0.2$ for thermal-like updrafts, we define c_z as

$$c_z = 0.2\left(1 - \frac{w_b}{w_c}\right). \quad (18)$$

The drag coefficient of 0.2 for thermal-like updrafts is consistent with the drag coefficient for high Reynolds number flow past a solid sphere and our assumption for c_x. This also gives consistent behavior with past numerical simulations as described below.

To obtain H, Eqs. (12), (16), and (17) are vertically integrated together using a simple Euler integration scheme. For instances of w_c, 0 m s^{-1}, we simply set $w_c = 0$ m s^{-1}. We define H as the highest instance of w_c. 0 m s^{-1}. To briefly demonstrate how shear will suppress thermal ascent rates and reduce H in our equation set, we apply it to an idealized sinusoidal profile of B defined as $B = 0.3\sin(2\pi z/8000\text{ m})\text{ s}^{-2}$ for $0 \le z \le 16000$ m, and $B = 0$ m s^{-2}

elsewhere, and with $R_0 = 500$ m (Figs. 2a,c), $R_0 = 1000$ m (Figs. 2b,d), $s = 5$ m s^{21} (6 km)^{21} (Figs. 2a,b), and $s = 25$ m s^{21} (6 km)^{21} (Figs. 2c,d). We compare solutions from the full equations to analogous solutions with the shear suppression effect turned off by setting $s = 0$ m s^{21} (6 km)^{21}. Vertical profiles of w_c from the full model show noticeable reductions in w_c and H, relative to when the shear suppression effect is excluded, that are generally largest when R is small and s is large. Solutions for U are also shown, which demonstrate that the thermal's U speed is a fraction of that of the environment at each height, resulting in substantial U which contributes to the shear suppression effect. This formulation gives a 30% reduction in H for 1-km-wide thermals experiencing a bulk wind difference (BWD) of 30 m s^{21} over a 9-km depth [consistent with the simulation results of Peters et al. (2019a)], relative to when Eq. (12) is integrated with the shear suppression effect entirely omitted.

b. Determining how the cloud will evolve in time

We next determine how R should evolve after the initial rising thermal. Because H and R are intrinsically connected via the link between R and entrainment-driven dilution [e.g., Eq. (7)], an increasing R with time in subsequent thermals should equate to an increase in H with time because thermals will progressively terminate at higher levels owing to reduced dilution. In contrast, a narrowing of R with time in subsequent thermals should correspond to a decrease in H because subsequent thermals will terminate at progressively lower heights. We assume that R is constant for a given thermal as it ascends from the LFC to H, which is supported by past modeling studies (Hernandez-Deckers and Sherwood 2016; Peters et al. 2019b; Morrison et al. 2021). Because a thermal achieves H after it has ascended, we consider H_i to correspond to R_{i21} for any time step index i. For instance, the first thermal which rises with R_0 achieves H_1, and this is used subsequently to determine R_1 for the next step. Thus for a given time step index i, to obtain H_{i11}, we evaluate Eq. (12) with R_i in place of R, and define H_{i11} as the highest instance of $w_{c,i} . 0$ m s^{21}.

Our method for obtaining R_i from H_i follows that of Peters et al. (2020b). First, we vertically integrate Eq. (9) from z = 0 to the height at which a rising thermal achieves its maximum w_c, w_{max}. The height of w_{max} is defined as sH_i, where $0 , s, 1$ is a constant that represents the ratio of the height of w_{max} to H_i. Radially integrating from r = 0 to r = R_i gives

$$u_r sH_i \Gamma \overline{w}_{cent} R_i \; 0: \quad \frac{1}{2} \quad (19)$$

updraft lateral boundary at$_r$ r = R_i between z = 0 and z = sH_i The quantity u is the average speed at which air crosses the and is therefore, by our definition, inflow. cloud-relative flow V_{CR} in the layer between$_r$ z = 0 and z = sH_i. Next, we assume that the inflow u corresponds with the

That is, V_{CR} within this layer enters the updraft on one side and a fraction of this air turns upward, so that only the fraction of air that does not turn upward exits the opposite side of the updraft. Furthermore, we assume that the fraction of air that turns upward, #, is constant in all situations. This assumption may seem overly restrictive; however, detailed analyses of cloud inflow in numerical simulations in Part II justifies this assumption. Note that we have not restricted inflow to be air with positive convective available potential energy (CAPE) [i.e., air within the effective inflow layer (EIL); Thompson et al. 2007]. In fact, our definition of inflow often includes a large percentage of air originating from above the EIL. This assumption is consistent with previous studies showing that updraft air originates within a much deeper layer than the EIL (Schiro et al. 2018), which is especially true for the air within the updraft that is close to its periphery (Nowotarski et al. 2020).

To connect V_{CR} to u_r, we assume that cloud motion C is predominantly driven by downstream advection, rather than propagation, during the developing stages of deep convection. Thus, we may define our cloud motion vector as the vertical average through the depth of the cloud, such that $C \approx 1/H_i \int_0 V_0 dz$. The vertical profile of the magnitude

$$\int_z^{zH_i}$$

of the background cloud-relative wind is $|V_{CR}(z)| = |V_{CR} = |V_0(z) 2C|$. For a linear zonal wind profile that is characterized by $u(z) = u_G 1 sz$, where u_G is the speed at ground level and s is constant,$_{CR}$ V_{CR} s z 2 H_i=2. Finally, in verti-$_i$ cally averaging V

between z = 0 and z = sH (i.e., the height of $_{CR}$ $_r$ rw_{max}), we obtain

$_{0\,CR}$ V_{CR} sH_i=2$_i$ ((s2 1)).

Using our assumed flow structure, we geometrically relate V to u using

$$u \quad \frac{2}{\#_{fp}} \quad V \quad \frac{\#sH}{\sin f df} \quad \frac{}{s2\,1}, \quad (20)$$

where the negative accounts for the fact that inflow should correspond to u_r dr=dt , 0. Using w_{cent} a$w_{max,i}$, we may combine Eqs. (19) and (20) to obtain an expression for the R_i of the next thermal emanating from the LFC:

$$R_i \approx \frac{\#ss H_i^2}{\pi a w_{max,i}} \left(1 - 2^{S}\right) \cdot \quad (21)$$

Equation (21) expresses a diagnostic relationship between R_i, H_i, and $w_{max,i}$ at time step index i. We may write this

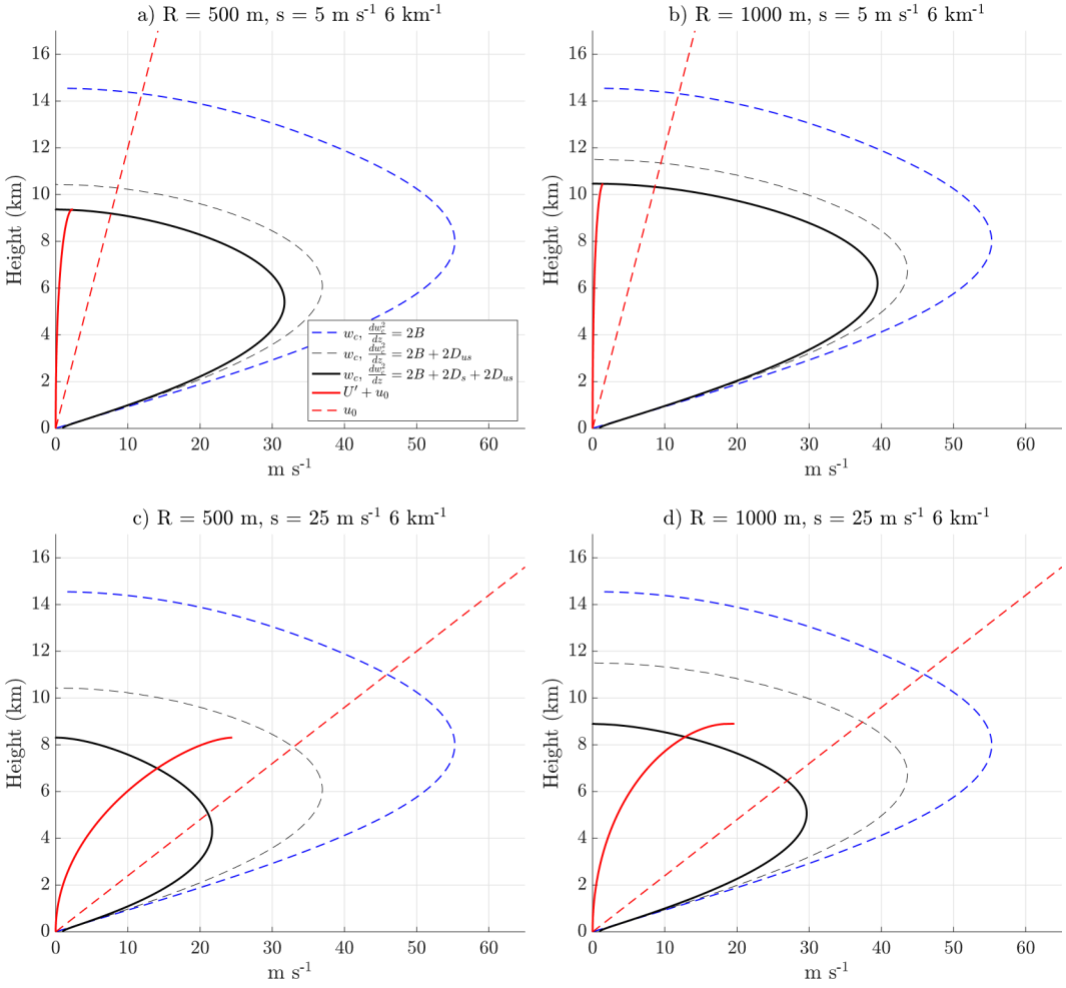

FIG. 2. w_c (black solid lines, m s^{21}) and U 1 u_0 (red solid lines, m s^{21}) applied to the simple B profile B 0:3 sin2pz=8000 m s^{22}. Black dashed lines show w_c with the shear-induced component of drag D_s neglected and the unsheared component of drag D_{us} retained (m s^{21}), blue dashed lines show w_c with all drag neglected (m s^{21}), and the red dashed lines show u_0 (m s^{21}). The degree to which shear suppressed thermal ascent rates is evident as the difference in the terminus heights of the solid black and dashed black lines.

equation in differential form by removing the i indices and taking d=dt, obtaining

$$\frac{dR}{dt} \approx \frac{\#ss}{\pi a} \left(1 - 2s\right) : \frac{d\, w_{Hmax2}}{dt} \quad (22)$$

Equation (22) reveals that for a cloud to widen with time, its ratio H^2/w_{max} must increase with time. In other words, the depth must increase at a sufficiently faster rate than the maximum vertical velocity for an increase in horizontal mass flux to equate to a widening cloud. Alternatively, if w_{max} were to increase sufficiently fast relative to H^2 to render $d H^2/w_{max}/dt > 0$ despite $dH/dt > 0$, the increase in horizontal inflow resulting from a deepening cloud would be only compensated by an increase in updraft speed while there would be a narrowing of the cloud.

A particular limitation of Eq. (21) is that in unsheared flow (i.e., $s \rightarrow 0$), R will vanish. This is a consequence of our assumption that all inflow is driven by V_{CR}, and the corresponding neglect of inflow that is locally induced by clouds' pressure perturbations. This assumption is extensively evaluated via analyses of trajectories in numerical simulations in section 4 of Part II, wherein it is shown that the locally induced component of inflow into nascent updrafts is small relative to the component of inflow associated with V_{CR} in moderately to strongly sheared environments. This assumption obviously cannot hold true for

weakly sheared or unsheared environments when $V_{CR} \rightarrow 0$. However, since Eq. (22) is first evaluated after the initial thermal with R_0 has ascended, our model still does permit convection to occur when s = 0. The model just does not allow the convection to persist beyond the rise of the initial thermal. This is actually quite consistent with past simulations of weakly sheared convection (Weisman and Klemp 1982; Peters et al. 2020d), which shows that deep convection only persists over a limited time scale (i.e., ,1 h) in the absence of external factors that continue to drive sub-LFC updrafts, such as cold pools. A theoretical justification for this assumption is provided in section 4 of Part II.

Because at any given time a developing cloud may be composed of a series of discrete thermals, there is conceivably a scenario where the horizontal motion of some thermals deviates from that of other portions of the cloud. This behavior may be prevalent for thermals near clouds that have "detached" from the main updraft and are sheared downstream (as is evident in Fig. 2c of Peters et al. 2019a). We assume the layer over which we average the ambient wind to estimate the advective component of cloud motion should exclude these "rogue" detached thermals. Consequently, we want to adjust Eq. (21) so that it only pertains to the vertically continuous layer of w . 0 m s^{21}.

For cloud that has vertically continuous ascending motion (i.e., a "plume-like" structure), we require that w_b . 0 m s^{21} for all w_c . 0 m s^{21}. In words, this means that for the entire vertical path over which a thermal has ascended, w at its bottom must be . 0 m s^{21}. This implies that the thermal is connected to the cloudy updraft below the thermal's base. We therefore define the height z_{wc} as the maximum height of w_c . 0 m s^{21}, and z_{wb} as the maximum height where w_b . 0 m s^{21}. Using these heights, the right-hand side of Eq. (21) is modified to give

$$R_i \;\; \frac{\quad}{z_{wbc}\,2\,\#ssH_{i2}\,(1\;2s)}, \qquad (23)$$

$$z_w \; pa w_{max,i}$$

where $0\#z_{wb}=z_{wc}$, 1 adjusts H_i to correspond to the maximum depth of continuous updraft.

c. Accounting for the influence of entrainment on R

Entrained air parcels do not mix uniformly throughout an updraft. Rather, parcels near the edge of an updraft will contain a larger percentage of environmental air in their mixture than parcels near the center of the updraft (Savre and Herzog 2019). In some cases, mixing may cause parcels near the updraft edge to become negatively buoyant due to the evaporation of condensate. These negatively buoyant mixtures are thought to be shed from the updraft through a process colloquially referred to as "buoyancy sorting" (Zhao and Austin 2003; Savre and Herzog 2019). The shedding of these negatively buoyant mixtures from cloud edge would be expected to reduce R.

Our strategy to account for these processes is inspired by Zhao and Austin (2003). First, we formally define MSE, which is necessary for calculating radial mixing properties, as

$$\mathrm{MSE} \equiv (1\;2\;q_t)c_{pd}\,1\,q_t c_l T\,1\,L_v q_v 2\,L_i q_i\,1\,gz, \qquad (24)$$

where q_t, q_v, and q_i are the total water, water vapor, and ice mass fractions of the updraft parcel, c_{pd} is the specific heat of dry air at constant pressure, c_l is the specific heat of liquid water, $L_v \equiv L_{v,trip}\,1\,T\,2\,T_{trip}(c_{pv}2\,c_l)$ is the latent heat of vaporization, $L_{v,trip}$ is a reference latent heat of vaporization at the triple point temperature T_{trip} = 273.15 K, $L_i \equiv L_{i,trip}\,1\,T\,2\,T_{trip}(c_l\,2\,c_i)$ is the latent heat of freezing, and $L_{i,trip}$ is a reference latent heat of freezing at T_{trip}. At this point, q_t, q_v, q_i, and T are all unknowns.

We obtain q_i using a simple mixed phase assumption akin to that of Bryan and Fritsch (2004). We define a parameter ν that is equal to 1 when T , 233.15 K, 0 when T . 273.15 K, and that varies linearly from 0 to 1 from T = 273.15 K to T = 233.15 K, respectively. Using ν, we require that $q_i \;\; \nu(q_t\;2\;q_v)$. Following Khairoutdinov and Randall (2003), we assume that $q_v \;\; (1\;2\;\nu)q_{s,v}1\nu q_{s,i}$, where $q_{s,v}$ and $q_{s,i}$ are the saturation mass fractions over liquid and ice, respectively, each calculated with Bolton's formulas. These assumptions relegate our unknowns to q_t and T.

To obtain q_t, we assume that it dissipates with height at the rate of «(i.e., neglecting sedimentation), such that

$$\frac{dq_t}{dz} \;\; 2«(q_t\,2\,q_{v,0}), \qquad (25)$$

where $q_{v,0}$ is the q_v of the background environment. The particular solution to Eq. (25) with $q_t(z_b) = q_{v,0}(z_b)$ at the parcel origin height z_b is

$$q_t(\;)z \;\; e^{\;(z2z_b)} q_{v,0}(z_b)\;1\;{}^{z}_{z_b}{}^{**}«q_{v,0}z^{*}e«(z^{*}2z_b)dz^{*}, \qquad (26)$$

which gives us q_t as a function of known quantities.

Our last task is to obtain T. The formula for B in Cloud Model 1 (CM1) (e.g., Bryan and Fritsch 2002; the model that is used in Part II) is

[2] We assume that the lateral mixing at height H/2 is approximately representative of the lateral mixing at other heights within the cloud. The theoretical model was relatively insensitive to reasonable variations in this height (i.e., 2H/3 and H/3).

$$B \equiv g\left(\frac{\theta - \theta_0}{\theta_0} + \left(\frac{R_v}{R_d} - 1\right)(q_v - q_{v,0}) - (q_t - q_{v,0})\right), \quad (27)$$

where u is potential temperature, and R_y and R_d are the specific gas constants for water vapor and dry air, respectively. If we assume that a rising parcel's pressure instantaneously adjusts to that of the horizontally invariant background environment p_0, then $(u2u_0)=u_0$ $(T\ 2\ T_0)=T_0$. Finally, we assume $q_y = q_{y,s}$, where $q_{y,s}$ is the saturation mass fraction. Since $q_{y,s}$ depends on T, we used an iterative approach to solve for T at height z using the B from Eq. (5).

At height H/2, the q_t and MSE at the updraft center are $q_{t,H=2}$ and $MSE_{H=2}$, respectively, and the values in the background environment at H/2 are $q_{y,0,H=2}$ and $MSE_{0,H=2}$, respectively.[2] We and $q_t(\ )r$ as the azimuthally averaged radial dependent distribu- ( ) also define r as the distance from the updraft center, and MSE r tions of MSE and q_t at height H/2. These radial distributions take the form

$$MSE\ r\tilde{}(\ ) \_\_r\ MSE_{H=2}\ 1\ \ 1\ 2\ \_\_r\ MSE_{0,H=2}, \quad (28)$$

R R

and

$$q\ \ _t(\ )r \_\_ q_{t,H=2}\ 1\ \ 1\ 2\_\_q_{y,0,H=2} \cdot (29)\ r\ r\ R \qquad R$$

In words, we have assumed that the percentage mixture of environmental air decreases linearly from 100% at r = R to 0% at r = 0 in a manner consistent with Zhao and Austin (2003). In using Eqs. (28) and (29), assuming that q_y q_s, and making use of Eq.( )(24), we solve for the radial distribution of temperature $T\ r_{\sim}$ at height H/2. To account for buoyancy sorting effects on R, we evaluate these equations to find the smallest value of r with negatively buoyant air (r_{nb}), and R is reduced to r_{nb} at the beginning of the next iteration step.

d. Selection of parameter values

We must assign values to the numerous constants in our model for later evaluation. For instance, the following variables are set to their "standard" values in CM1: $k^2 = 0.18$, $P_r = 1/3$, $L_{y,ref}$ 2:501 3 10_6 J kg_{21}, $L_{i,0} = 3.33$ 3 10_5 J kg_{21}, $c_{pd} = 1005$ J kg^{21} K^{21}, $c_{py} = 1870$ J kg^{21} K^{21}, $c_l = 4190$ J kg^{21} K^{21}, and $c_i = 2106$ J kg^{21} K^{21}. We adopt these values for consistency with the comparison of the theoretical model against numerical simulations in Part II. To remain consistent with assumed linear radial profiles used to formulate buoyancy sorting, we set $\overline{a}$ 1=3 because it can be shown that $\overline{a\ c=c_c}$ 1=3 for an arbitrary quantity c with a linear radial distribution, a value c_c at the updraft center, and a value of 0 at the updraft edge. Somewhat arbitrarily, the entire quantity s(1 2s)=a in Eq. (21) is set to 0.5, which implies that s = 0.78. This value for s}the ratio of the height of w_{max} to H}is consistent with the value of 0.7 found in the two-dimensional numerical simulations of Peters (2016). We ran numerous sensitivity tests with alterations to these parameters, and found that the solutions to the model that will be shown in forthcoming sections were qualitatively consistent over a wide range of plausible parameter values. Finally, and for simplicity, # is set to 1 indicating that all V_{CR} turns upward into the updraft.

4. Example solutions of the theoretical model

a. Integrating the theoretical model with analytically generated environmental profiles

We first evaluated our theoretical model with the well-known analytic environmental sounding used by Weisman and Klemp (1982) (hereafter the WK82 profile). The water vapor mixing ratio in the lowest part of the atmosphere, r_{PBL}, was set to a constant value to emulate the presence of a well-mixed PBL. We used r_{PBL} values of 12 and 16 g kg^{21}, corresponding to most unstable CAPE (MUCAPE) of 2568 and 3556 J kg^{21}, respectively[3] (see Fig. 1 in Part II for reference). Because RH above the PBL is a key influencing factor on DCI (Derbyshire et al. 2004; Nelson et al. 2021; Morrison et al. 2022), we also tested a range of constant RH values above 1.5 km from 10% to 90% at intervals of 10%.[4] These constant RH values were used to determine the water vapor mixing ratios and mass fractions above 3 km in lieu of the original formula from Weisman and Klemp (1982). Our theoretical model only required the specification of a single shear magnitude s that is constant with height, and we therefore only considered singular values of s instead of constructing vertically varying shear profiles. We initialized with s = 0 m s^{21} $(6\ km)^{21}$ through s = 45 m s^{21} $(6\ km)^{21}$, at intervals of 5 m s^{21} $(6\ km)^{21}$. We also initialized with R_0 ranging from 100 to 3000 m, at intervals of 100 m and RH ranging from 10% to 90% at intervals of 10%. Finally, we integrated the model until a steady state R was a achieved, or until R settled to zero.

b. Temporal behavior of the theoretical model

Time series of R illustrate the temporal behavior of our theoretical model. For small s, steady updrafts are not possible. In these situations, R declined from its initial values for the entire range of R_0 (e.g., Figs. 3a–d). For comparatively large s, a contrasting behavior of R is apparent (e.g., Figs. 3e–i). Time series with small R_0 featured a steady decrease in R with time, much like in the case of the environments with smaller s. However, in time

series with larger R_0, R evolved toward a steady nonzero value (e.g., Figs. 3f–i). This evolution toward a steady value occurs because as R increases, the maximum buoyancy of the updraft B_m approaches the buoyancy of an undiluted air parcel B_{UD}. Eventually, increases in R stop having an appreciable effect on B_m because B_m already represents that of an undiluted parcel. Because the updraft depth H is strongly dependent on B_m, H will become approximately constant once B_m becomes approximately constant. At this point the updraft is no longer deepening, changing its motion, changing its V_{CR}, or changing its R and thus the positive feedback among these quantities ceases, leading to a steady state.

There is a sharp cutoff in R_0, below which no sustained updrafts occur, and above which, steady updrafts occur. This is indicated by the discontinuous jump from a final R (hereafter R_F) of zero when R_0 is smaller than the cutoff, to a large R_F when R_0 is larger than the threshold (e.g., Figs. 3g–i). For instance, there are numerous instances of R_0 that were only 100 m different from each other, wherein the larger value resulted in a steady updraft and the smaller value did not.

Past the first time step, time series of H (Fig. 4), V_{CR} (Fig. 5), and w_{max} (Fig. 6) behave in a similar manner to R. For instance, beyond the initial increases in these quantities at the first time step, they increase with time along curves for which R increases with time and decrease with time along curves for which R decreases with time. This behavior exemplifies our hypothesis, in that updrafts with increasing R become deeper, establish larger inflow, and achieve faster w, whereas updrafts with decreasing R become shallower, establish smaller inflow, and experience a reduction in w with time.

c. Bulk analysis of the theoretical model behavior

Next, we investigate theoretical model–predicted R_F as a function of R_0, s, RH, and r_{PBL} that are input into the theoretical model. Recall that steady self-sustaining updrafts correspond to R_F Þ 0 km. In sufficiently dry free-tropospheric environments, steady

[3] CAPE was computed by lifting a parcel adiabatically using the method outlined in Peters et al. (2022a).

[4] RH was computed with respect to liquid and ice using the formula from appendix A of Peters and Chavas (2021).

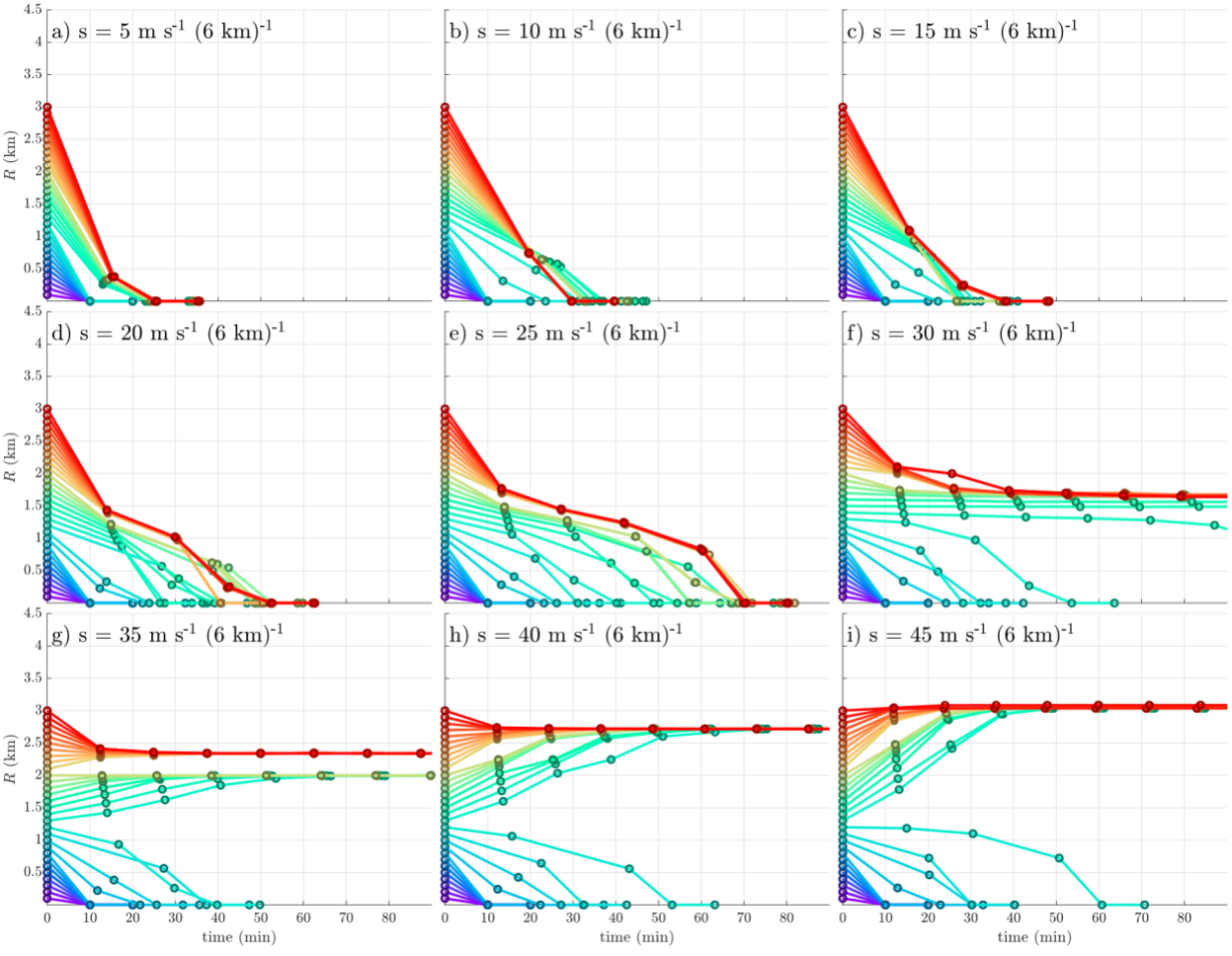

FIG. 3. Time series of R (km) from our theoretical model evaluated with r_{PBL} = 16 g kg^{21} and RH = 50%. The color of lines corresponds to the R_0, with R_0 corresponding to the vertical position of a given line as it intersects the y axis. Each panel corresponds to a different shear value. Each dot represents a single output time from the theoretical model.

self-sustaining updrafts are not possible with the parameter combinations we have investigated. For instance, $R_F = 0$ km for all parameter combinations with $r_{PBL} = 12$ g kg^{21} and RH , 50% (Figs. 7a–d), and with $r_{PBL} = 16$ g kg^{21} and RH , 30% (Figs. 8a,b). Once above these thresholds in RH, and as we consider progressively larger RH (Figs. 7e–i, 8c–i), steady updrafts become possible over an increasingly large fraction of the parameter space, to the point where nearly all combinations of s and R_0 achieve steady updrafts with RH = 90% for both of the r_{PBL} values considered (Figs. 7i, 8i). This trend indicates a strong influence of free-tropospheric RH on whether or not steady self-sustaining updrafts develop, and occurs because entraining dry free-tropospheric air has a much more negative effect on updraft B than entraining comparatively moist freetropospheric air.

It is also apparent that r_{PBL} influences the likelihood of steady self-sustaining updrafts, by means of the effect of r_{PBL} on B_{UD} in the thermodynamic profiles we have examined. For instance, for a given RH, steady self-sustaining updrafts occur over a much larger portion of the s versus R_0 parameter space when $r_{PBL} = 16$ g kg^{21} (Fig. 8) than when $r_{PBL} = 12$ g kg^{21} (Fig. 7). This trend occurs because when r_{PBL} is large, B_{UD} will increase at a faster rate with height requiring more entrainment-driven dilution to suppress updraft growth, than in the situation where r_{PBL} is small and B_{UD} increases comparatively slowly with height.

Another noteworthy result is the tendency for R_F to remain nearly constant over a range of R_0, in regions of the parameter space where R_F Þ 0 km. This suggest that for a given s, RH, and r_{PBL}, clouds with a range of initial updraft sizes will all evolve toward a similar R_F. Similar behavior is observed in numerical simulations (see Part II), and predicted in the theoretical analyses of Peters et al. (2019b). Perhaps the most striking feature of the theoretical model, however, is the sharp threshold in R_0 that determines whether or not a steady self-sustaining updraft occurs. Above this threshold in R_0, all R_F share a common value for a given s, RH, and r_{PBL}. Below this threshold, all $R_F = 0$ km. This trend suggests that the behavior identified in time series in the previous subsection occurs over a wide range of environments.

There are large expanses of the parameter space where deep convection is possible, but steady self-sustaining updrafts are not. We identify these regions through an analysis of H_{max}, which is

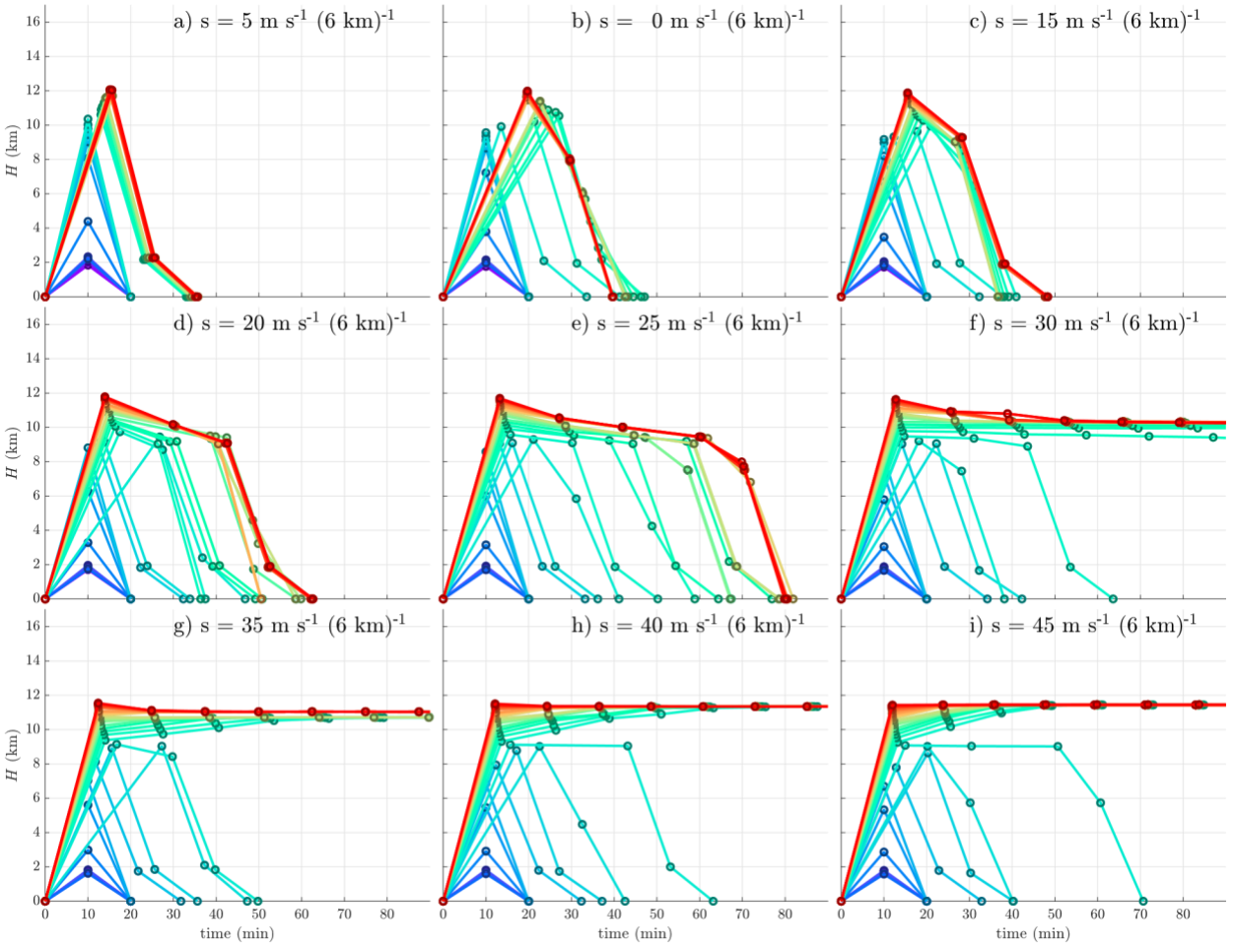

FIG. 4. As in Fig. 3, but showing time series of H (km).

the maximum H achieved at any time during the theoretical model integration for a given input parameter combination. As a quantitative measure of whether an updraft has achieved DCI, we introduce the quantity $h_{rat} \equiv H_{max}=H_{UD}$, where H_{UD} is the H_{max} for an undiluted updraft (i.e., « = 0). Conceptually, h_{rat} represents the fraction a given updraft achieves of the maximum possible updraft depth. We require h_{rat} to exceed 0.8 at some time when integrating the theoretical model for DCI to have occurred. This threshold is somewhat arbitrary, but the interpretation of our results is unchanged for alternative h_{rat} thresholds ranging from 0.5 to 0.9.

Unsurprisingly, h_{rat} was strongly dependent on both R_0 and RH. These trends are evident as an increase in h_{rat} for increasing R_0 in each individual panel of Figs. 7 and 8, and an increase in h_{rat} for fixed values of R_0 and s as RH increased (i.e., as one progresses from Figs. 7a–i to Figs. 8a–i). This behavior echoes the results of Morrison et al. (2022), in that larger low-level updrafts and a moister environment above the LFC make DCI more favorable.

The influence of s on the behavior of h_{rat} is quite complex. In portions of the parameter space where steady updrafts are not possible, s and h_{rat} display an inverse relationship, such that stronger s equates to shallower updrafts and a decreased likelihood of DCI. This negative correspondence between s and DCI is reflected by a general upward slope in the h_{rat} = 0.8 threshold toward larger R_0 as one moves to the right in each panel. In particular, when RH was small, this trend applied for nearly all s and R_0 (e.g., Figs. 7a–f; 8a–c).

As RH, s, and r_{PBL} increase, steady self-sustaining updrafts become possible over an increasingly large percentage of the parameter space (e.g., Figs. 7g–i; 8d–i). In these instances, the relationship between s and h_{rat} is not monotonic. For instance, consider the situation with r_{PBL} = 16 g kg^{21}, RH = 70%, and R_0 = 0.75 km (Fig. 8g). In this situation, h_{rat} initially decreases with increasing s. However, beyond s ≈ 20 m s^{21} (6 km)^{21}, h_{rat} abruptly exceeds 0.8 as steady updrafts become possible, and does not drop below that value as s increases beyond this threshold. This means that above a certain s threshold, the negative effects of s on DCI abruptly cease, whereas below that threshold s is severely detrimental to DCI. Similar behavior is evident among other combinations of RH and r_{PBL}.

To isolate processes related to s in our theoretical model, we

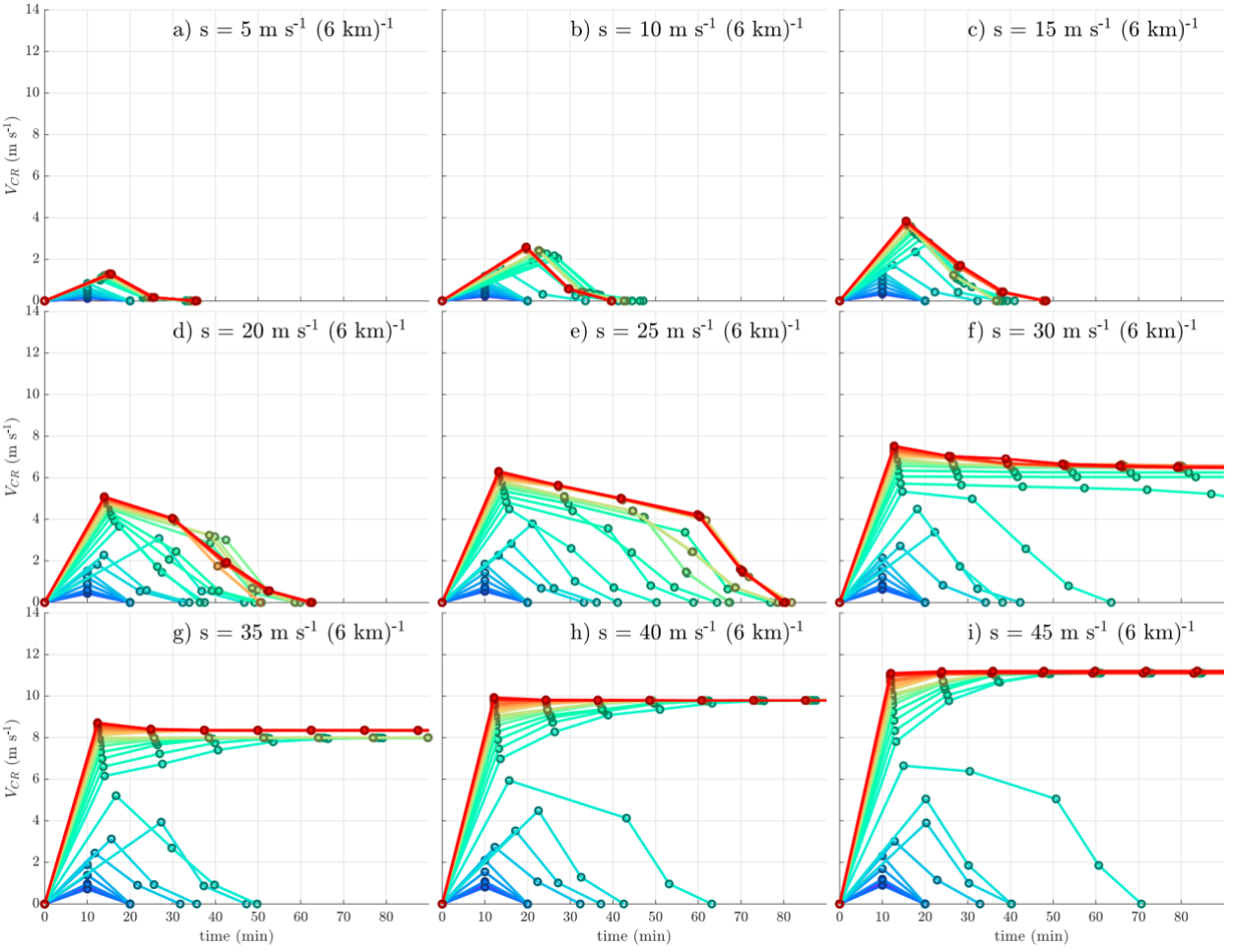

FIG. 5. As in Fig. 3, but showing time series of V_{CR} (m s^{21}).

compare h_{rat} for a given value of s to $h_{rat,ns}$ computed with s set to 0 (where the subscript "ns" stands for "no shear"). This sensitivity test gives us a baseline for the maximum h_{rat} an updraft would achieve for given values of R_0, RH, and r_{PBL} in the absence of environmental shear. For nearly all of the parameter space considered, $h_{rat,ns}$ $ h_{rat}, implying that s generally reduces updraft depth (Figs. 9 and 10). The reduction in h_{rat} by s is generally minimal in regions of the parameter space where steady updrafts develop, and much larger in regions of the parameter space where updrafts are transient. We note that s also seems to increase the R_0 required for deep convection to occur when steady updrafts do not occur, as indicated by a shift in the 0.8 threshold toward larger R_0 in Figs. 9 and 10.

In regions of the parameter space where steady updrafts do not occur (Figs. 9 and 10), s reduces the depth of updrafts relative to theoretical model solutions with s absent. This effect is generally most pronounced with large RH, small-tomedium R_0 (i.e., R_0 , 1.5 km), and when s was large. The apparent positive correspondence between RH and the s suppression effect is somewhat counterintuitive, given that one would expect updrafts to be less susceptible to entrainmentdriven dilution when RH is large. However, as RH becomes larger, buoyant updrafts become possible for increasingly small R_0. At the same time, updrafts with small R experience greater s suppression than updrafts with larger R. Thus, the region of the parameter space (small R_0) that is most susceptible to the s suppression is only becoming "activated" with large RH.

5. Summary and conclusions

This article addresses a novel hypothesis for the role of vertical wind shear in the onset of deep convection, referred to as deep convection initiation (DCI). In this hypothesis, nascent convective updrafts of sufficient width increase their updraftrelative inflow upon encountering environmental wind shear. Updrafts widen because of this increased inflow, which reduces their susceptibility to entrainment-driven dilution. From this process, clouds can progressively "root" into a deeper steering current, furthering this positive feedback cycle. Updrafts eventually achieve a steady width, w, depth, and motion. Under situations for which

progressive rooting occurs, the deleterious effects of shear-induced downward pressure gradient accelerations are counteracted by causing them to widen beyond what would have been possible without shear, and without an external factor that provides sustained low-level lifting.

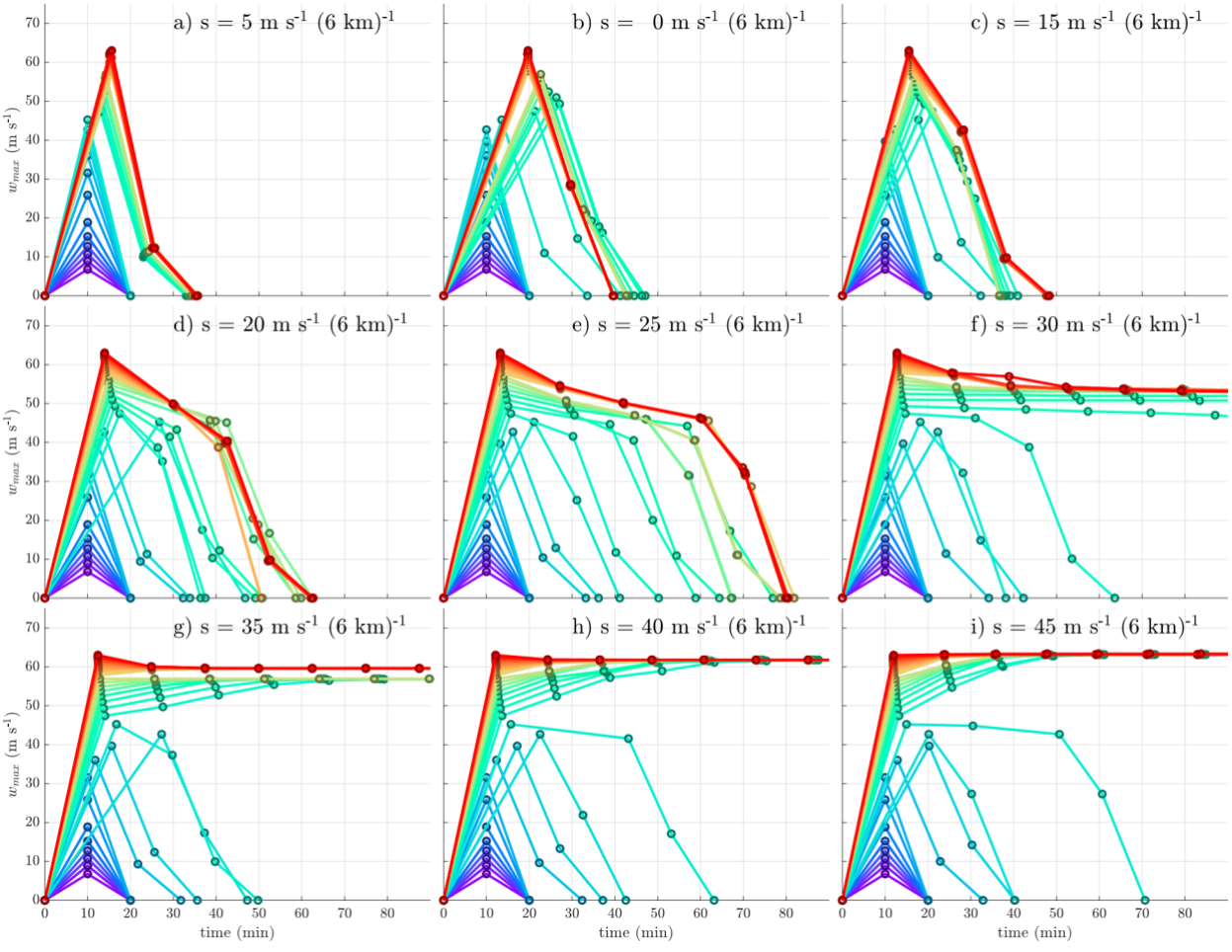

FIG. 6. As in Fig. 3, but showing time series of w_{max} (m s^{21}).

To quantitatively explore this hypothesis in a range of atmospheric environments, we developed a theoretical model that was based on simplifications of the equations of atmospheric motion and thermodynamics, and analyzed the model's behavior. This model predicts the temporal evolution of updraft width, depth, and w given an initial environmental profile and updraft width. We presented solutions to this model in a parameter space characterized by variations in initial updraft width, shear magnitude, environmental RH, and CAPE (specifically through variations in the PBL water vapor mixing ratio). Conclusions from our analysis of the behavior of this theoretical model over a range of analytic environmental profiles are as follows:

- The theoretical model suggests that certain conditions will lead to the development of steady self-sustaining updrafts. These conditions require sufficiently large initial updraft widths, r_{PBL} (and by extension, CAPE), and RH. In these cases, the suppressing effects of shear on updraft depth are counteracted by a widening and deepening of the updraft with time. Furthermore, shear actually facilitates the robustness and longevity of updrafts
- There is often an initial updraft width threshold, above which steady updrafts develop, and below which steady updrafts cannot exist. The exact threshold resulting in bifurcation is dependent on the r_{PBL} (and by extension, CAPE), RH, and shear.
- Theoretical model solutions suggest that for a given shear magnitude, initial updrafts with a large range of initial widths will all evolve toward the same steady state width over time. This is a behavior that has been previously observed in cloud-resolving simulations (Peters et al. 2019b), and is consistent with the behavior of the simulations analyzed in Part II.
- For environmental conditions that do not support progressive rooting, shear generally contributes to failed DCI.

Caveats and future work

Our hypothesis assumes that air parcels have reached their LFCs. We have not addressed the need for air parcels to

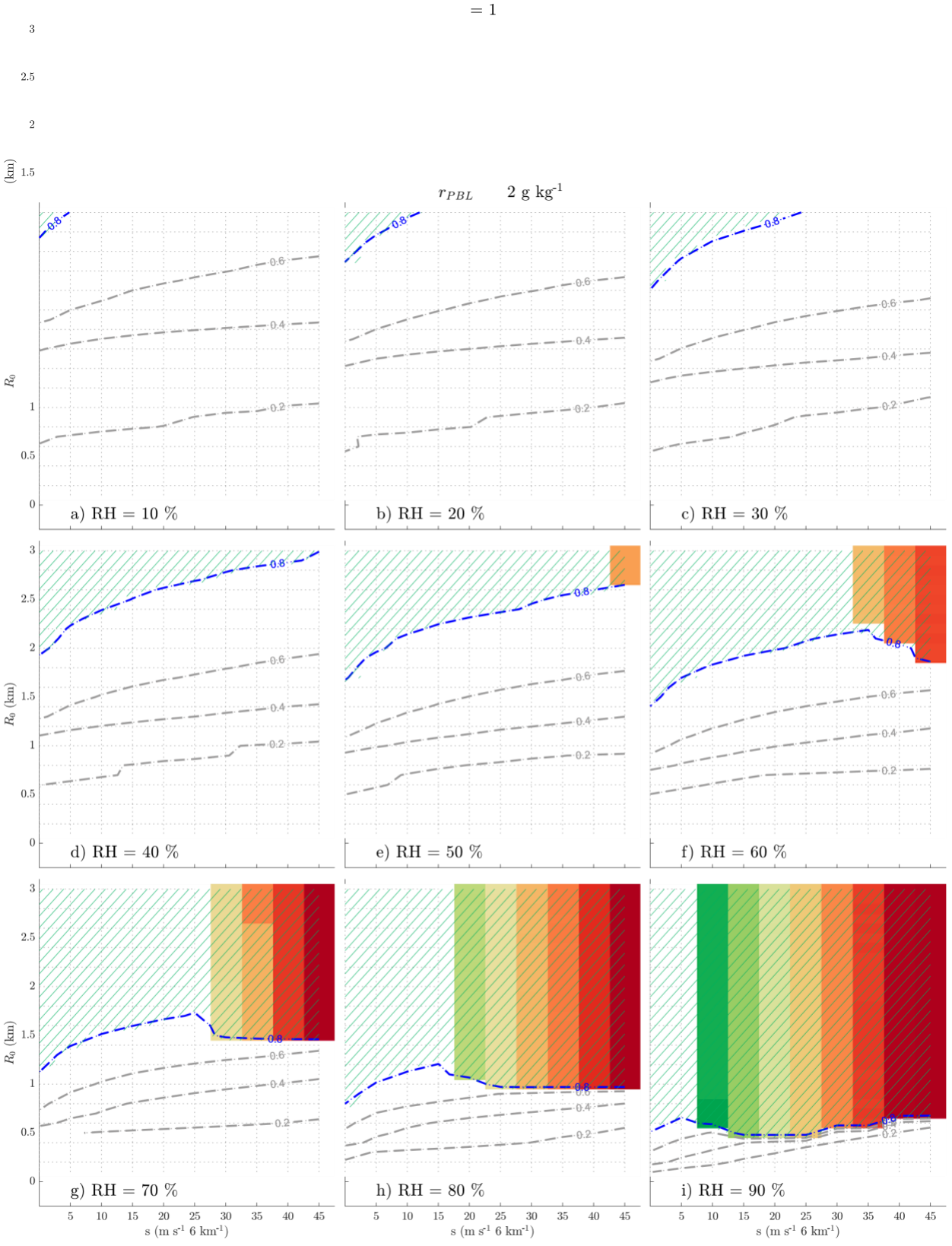

FIG. 7. Theoretical model solutions with r_{PBL} = 12 g kg^{21} and various $= 1$ RH % (panels), s [x axes, m s^{21} (6 km)^{21}], and R_0 (y axes, km) 3 combinations. Plots show temporal maximum in h_{rat} (contours) with the 0.8 threshold for DCI (dashed blue) and R_F (km, shading, numbers). Unshaded regions correspond to an R of 0 by the 20th time step. Green hatched regions indicate successful DCI.

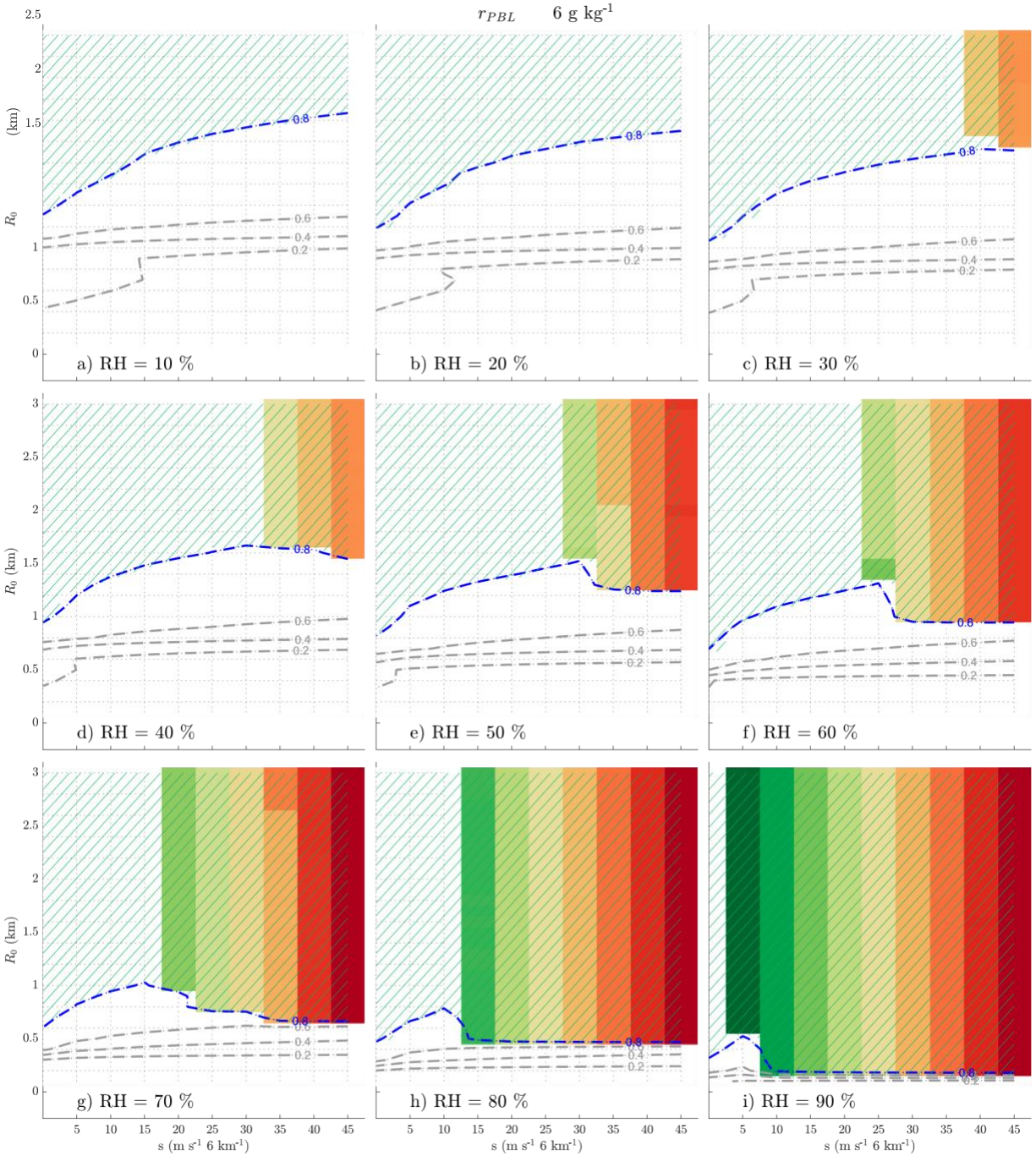

FIG. 8. As in Fig. 7, but with r_{PBL} = 16 g kg^{21}.

overcome CIN prior to reaching their LFCs. We acknowledge that this factor likely strongly influences DCI. Addressing this CIN related issue requires assumptions about the dynamics of updrafts in the sub-LFC layer, and is left to future work. However, our model may help elucidate processes supporting or inhibiting DCI in cases when CIN has been effectively eliminated.

It should also be noted that real atmospheric environments feature substantial spatiotemporal variability, whereas our theoretical model assumes a fixed background environment.

A prime example is when DCI occurs in the vicinity of a mountain range. In addition to directly providing sustained sub-LFC ascent to trigger updrafts, upslope flow driven by mountain solenoidal circulations has been shown to enhance low-level V_{CR} (Mulholland et al. 2019, 2020; Marquis et al. 2021). Another example is the development of the plains lowlevel jet in the evening, which may also enhance low-level V_{CR} (Coffer and Parker 2015). Both of these features likely influence whether steady updrafts are possible, but are not encapsulated by the linear-with-height temporally invariant wind profiles used here.

We emphasize that readers should not focus on the specific thresholds for successful or failed DCI, or the exact values of the quantitative measures of updraft properties that are predicted by our model. These specific thresholds and values are likely to vary depending on details of a given atmospheric

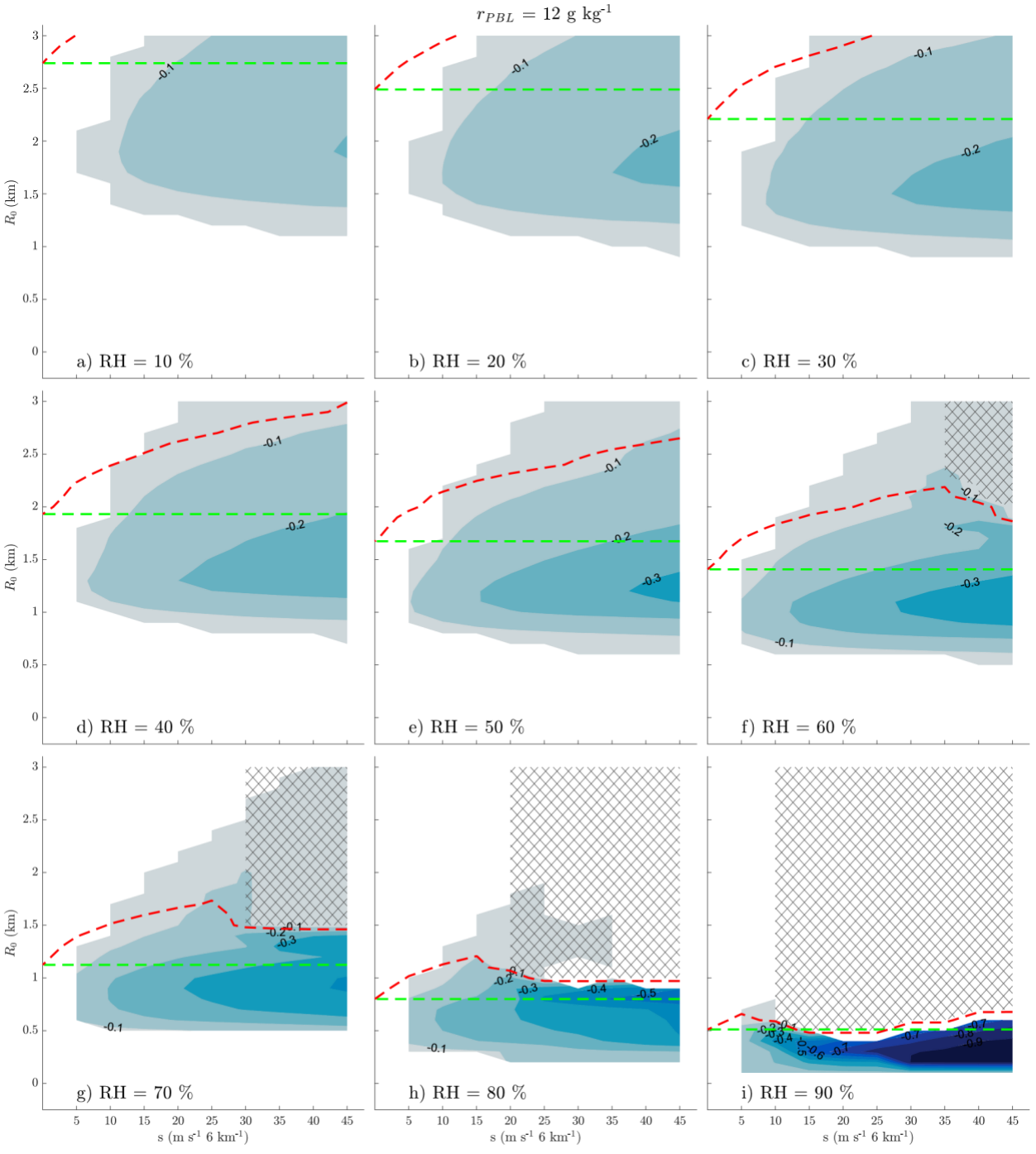

FIG. 9. Comparisons of theoretical model solutions with shear effects included, to a solution with s = 0 m s^{21} (6 km)^{21} with r_{PBL} = 12 g kg^{21}. Blue shading: h_{rat}–$h_{rat,ns}$ (see black number labels for values; note that this is unitless). The h_{rat} = 0.8 and $h_{rat,ns}$ = 0.8 contours are shown in red dashed and green dashed, respectively. Hatched areas indicate regions where steady self-sustaining updrafts are predicted by the theoretical model. The panel layout is as in Fig. 7.

profile, and/or the parameter settings in the model. A more important "take-home" insight from our analysis is the qualitative behaviors outlined in the conclusions above. For instance, how the likelihood of DCI changes with varying s, RH, r_{PBL} (and by extension, CAPE), and R_0. With that being said, future work may attempt to tune the parameter values used in our model so that it best emulates reality and/or cloud simulations in a quantitative manner. If such a tuning exercise were successful, this theoretical model could potentially be used in a cumulus parameterization scheme to guide a convective trigger function, and/or to predict convective updraft properties. This simplified model may also be a useful tool to aid forecasters in interpreting model output.

Acknowledgments. J. Peters's and J. Mulholland's efforts were supported by National Science Foundation (NSF) Grants AGS-1928666 and AGS-1841674, and the Department of Energy

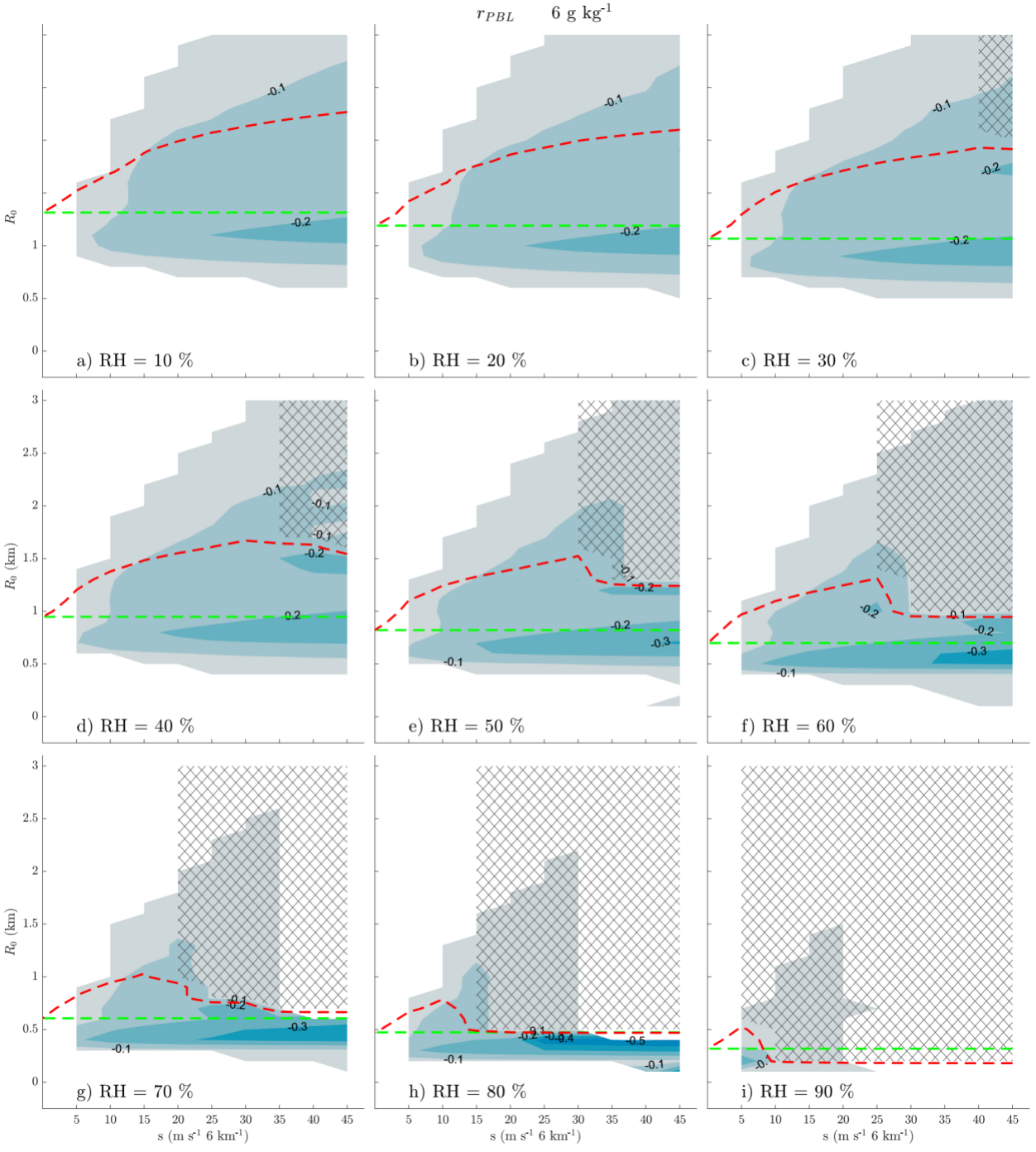

FIG. 10. As in Fig. 9, but with r_{PBL} = 16 g kg^{21}.

Atmospheric System Research (DOE ASR) Grant DE-SC0000246356. H. Morrison was supported by DOE ASR Grant DE-SC0020104. J. Marquis's and T. Nelson's efforts were supported by NSF Grant AGS-1661707. J. Marquis was also supported by DOE's Science Biological and Environmental Research as part of the ASR program, with work conducted at the Pacific Northwest National Laboratory. C. Nowotarski's

efforts were supported by NSF Grant AGS-1928319. The National Center for Atmospheric Research is sponsored by NSF. We thank three anonymous peer reviewers for their helpful feedback, which greatly improved the manuscript.

Data availability statement. All scripts and namelists used to generate the data for this study are available via Figshare at https://figshare.com/articles/dataset/DCI_STUDY/14515560.

REFERENCES

Betchold, P., J. P. Chaboureau, and A. Beljaars, 2004: The simulation of the diurnal cycle of convective precipitation over land in a global model. Quart. J. Roy. Meteor. Soc., 130, 3119–3137, https://doi.org/10.1256/qj.03.103.

Bryan, G. H., and J. M. Fritsch, 2002: A benchmark simulation for moist nonhydrostatic numerical models. Mon. Wea. Rev., 130, 2917–2928, https://doi.org/10.1175/1520-0493(2002)130,2917:ABSFMN.2.0.CO;2.

}}, and }}, 2004: A reevaluation of ice–liquid water potential temperature. Mon. Wea. Rev., 132, 2421–2431, https://doi.org/10.1175/1520-0493(2004)132,2421:AROIWP.2.0.CO;2.

Christopoulos, C., and T. Schneider, 2021: Assessing biases and climate implications of the diurnal precipitation cycle in climate models. Geophys. Res. Lett., 48, e2021GL093017, https://doi.org/10.1029/2021GL093017.

Coffer, B. E., and M. D. Parker, 2015: Impacts of increasing lowlevel shear on supercells during the early evening transition. Mon. Wea. Rev., 143, 1945–1969, https://doi.org/10.1175/MWRD-14-00328.1.

Collier, J. C., and K. P. Bowman, 2004: Diurnal cycle of tropical precipitation in a general circulation model. J. Geophys. Res., 109, D17105, https://doi.org/10.1029/2004JD004818.

Covey, C., P. J. Gleckler, C. Doutriaux, D. N. Williams, A. Dai, J. Fasullo, K. Trenberth, and A. Berg, 2016: Diurnal cycle of tropical precipitation in a general circulation model. J. Climate, 29, 4461–4471, https://doi.org/10.1175/JCLI-D-15-0664.1.

Dai, A., 2006: Precipitation characteristics in eighteen coupled climate models. J. Climate, 19, 4605–4630, https://doi.org/10.1175/JCLI3884.1.

}}, F. Giorgi, and K. Trenberth, 1999: Observed and modelsimulated diurnal cycles of precipitation over the contiguous United States. Geophys. Res. Lett., 104, 6377–6402, https://doi.org/10.1029/98JD02720.

Damiani, R., and Coauthors, 2008: The Cumulus, Photogrammetric, In Situ, and Doppler Observations experiment of 2006. Bull. Amer. Meteor. Soc., 89, 57–73, https://doi.org/10.1175/BAMS89-1-57.

Davies-Jones, R., 2002: Linear and nonlinear propagation of supercell storms. J. Atmos. Sci., 59, 3178–3205, https://doi.org/10.1175/1520-0469(2003)059,3178:LANPOS.2.0.CO;2.

Derbyshire, S. H., I. Beau, P. Bechtold, J.-Y. Grandpeix, J.-M. Piriou, J.-L. Redelsperger, and P. M. M. Soares, 2004: Sensitivity of moist convection to environmental humidity. Quart. J. Roy. Meteor. Soc., 130, 3055–3079, https://doi.org/10.1256/qj.03.130.

Doswell, C. A., III, and P. M. Markowski, 2004: Is buoyancy a relative quantity? Mon. Wea. Rev., 132, 853–863, https://doi.org/10.1175/1520-0493(2004)132,0853:IBARQ.2.0.CO;2.

Grabowski, W. W., and T. L. Clark, 1993: Cloud-environment interface instability. Part III: Direct influence of environmental shear. J. Atmos. Sci., 67, 3821–3828, https://doi.org/10.1175/ 1520-0469(1993)050,3821:CEIIPI.2.0.CO;2.

Hernandez-Deckers, D., and S. C. Sherwood, 2016: A numerical investigation of cumulus thermals. J. Atmos. Sci., 73, 4117–4136, https://doi.org/10.1175/JAS-D-15-0385.1.

}}, and }}, 2018: On the role of entrainment in the fate of cumulus thermals. J. Atmos. Sci., 75, 3911–3924, https://doi.org/10.1175/JAS-D-18-0077.1.

Houston, A. L., and D. Niyogi, 2007: The sensitivity of convective initiation to the lapse rate of the active cloud bearing layer. Mon. Wea. Rev., 135, 3013–3032, https://doi.org/10.1175/MWR3449.1.

Jeevanjee, N., 2017: Vertical velocity in the gray zone. J. Adv. Model. Earth Syst., 9, 2304–2316, https://doi.org/10.1002/2017MS001059.

Kain, J. S., and J. M. Fritsch, 1990: A one-dimensional entraining/detraining plume model and its application in convective parameterization. J. Atmos. Sci., 47, 2784–2802, https://doi.org/10.1175/1520-0469(1990)047,2784:AODEPM.2.0.CO;2.

Khairoutdinov, M., and D. A. Randall, 2003: Cloud resolving modeling of the ARM summer 1997 IOP: Model formulation, results, uncertainties, and sensitivities. J. Atmos. Sci., 60, 607–625, https://doi.org/10.1175/1520-0469(2003)060,0607:CRMOTA.2.0.CO;2.

}}, and }}, 2006: High-resolution simulation of shallow-to-deep convection transition over land. J. Atmos. Sci., 63, 3421–3436, https://doi.org/10.1175/JAS3810.1.

Kirshbaum, D. J., and A. L. M. Grant, 2012: Invigoration of cumulus cloud fields by mesoscale ascent. Quart. J. Roy. Meteor. Soc., 138, 2136–2150, https://doi.org/10.1002/qj.1954.

}}, and D. N. Straub, 2019: Linear theory of shallow convection in deep, vertically sheared atmospheres. Quart. J. Roy. Meteor. Soc., 145, 3129–3147, https://doi.org/10.1002/qj.3609.

Klemp, J. B., 1987: Dynamics of tornadic thunderstorms. Annu. Rev. Fluid Mech., 19, 369–402, https://doi.org/10.1146/annurev.fl.19.010187.002101.

Kuang, Z., and C. S. Bretherton, 2006: A mass-flux scheme view of a high-resolution simulation of a transition from shallow to deep cumulus convection. J. Atmos. Sci., 63, 1895–1909, https://doi.org/10.1175/JAS3723.1.

Kurowski, M. J., K. Suselj, W. W. Grabowski, and J. Teixeira, 2018: Shallow-to-deep transition of continental moist convection: Cold pools, surface fluxes, and mesoscale organization. J. Atmos. Sci., 75, 4071–4090, https://doi.org/10.1175/JAS-D18-0031.1.

Marion, G. R., and R. J. Trapp, 2019: The dynamical coupling of convective updrafts, downdrafts, and cold pools in simulated supercell thunderstorms. J. Geophys. Res. Atmos., 124, 664– 683, https://doi.org/10.1029/2018JD029055.

Markowski, P., and Y. Richardson, 2010: Mesoscale Meteorology in Midlatitudes. Wiley-Blackwell, 430 pp.

Marquis, J. N., A. C. Varble, P. Robinson, T. C. Nelson, and K. Friedrich, 2021: Low-level mesoscale and cloud-scale interactions

promoting deep convection initiation. Mon. Wea. Rev., 149, 2473–2495, https://doi.org/10.1175/MWR-D-20-0391.1.

McCarthy, J., 1974: Field verification of the relationship between entrainment rate and cumulus cloud diameter. J. Atmos. Sci., 31, 1028–1039, https://doi.org/10.1175/1520-0469(1974)031,1028:FVOTRB.2.0.CO;2.

Morrison, H., 2016: Impacts of updraft size and dimensionality on the perturbation pressure and vertical velocity in cumulus convection. Part I: Simple, generalized analytic solutions. J. Atmos. Sci., 73, 1441–1454, https://doi.org/10.1175/JAS-D15-0040.1.

}}, 2017: An analytic description of the structure and evolution of growing deep cumulus updrafts. J. Atmos. Sci., 74, 809–834, https://doi.org/10.1175/JAS-D-16-0234.1.

}}, and J. M. Peters, 2018: Theoretical expressions for the ascent rate of moist convective thermals. J. Atmos. Sci., 75, 1699–1719, https://doi.org/10.1175/JAS-D-17-0295.1.

}}, }}, W. M. Hannah, A. C. Varble, and S. E. Giangrande, 2020: Thermal chains in ascending moist updrafts: Part I: Theoretical description. J. Atmos. Sci., 77, 3637–3660, https://doi.org/10.1175/JAS-D-19-0243.1.

}}, }}, and S. C. Sherwood, 2021: Comparing growth rates of simulated moist and dry convective thermals. J. Atmos. Sci., 78, 797–816, https://doi.org/10.1175/JAS-D-20-0166.1.

}}, }}, K. K. Chandakar, and S. C. Sherwood, 2022: Influences of environmental relative humidity and horizontal scale of subcloud ascent on deep convective initiation. J. Atmos. Sci., 79, 337–359, https://doi.org/10.1175/JAS-D-21-0056.1.

Morton, B. R., G. I. Taylor, and J. S. Turner, 1956: Turbulent gravitational convection from maintained and instantaneous sources. Proc. Roy. Soc. London, 74, 375–392, https://doi.org/10.1098/rspa.1956.0011.

Moser, D. H., and S. Lasher-Trapp, 2017: The influence of successive thermals on entrainment and dilution in a simulated cumulus congestus. J. Atmos. Sci., 74, 375–392, https://doi.org/10.1175/JAS-D-16-0144.1.

Mulholland, J. P., S. W. Nesbitt, and R. J. Trapp, 2019: A case study of terrain influences on upscale convective growth of a supercell. Mon. Wea. Rev., 147, 4305–4324, https://doi.org/10. 1175/MWR-D-19-0099.1.

}}, }}, }}, and J. M. Peters, 2020: The influence of terrain on the convective environment and associated convective morphology from an idealized modeling perspective. J. Atmos. Sci., 77, 3929–3949, https://doi.org/10.1175/JAS-D19-0190.1.

}}, J. M. Peters, and H. Morrison, 2021: How does vertical wind shear influence entrainment in squall lines? J. Atmos. Sci., 74, 1931–1946, https://doi.org/10.1175/JAS-D-20-0299.1.

Nelson, T. C., J. Marquis, A. Varble, and K. Friedrich, 2021: Radiosonde observations of environments supporting deep moist convection initiation during RELAMPAGO-CACTI. Mon. Wea. Rev., 149, 289–309, https://doi.org/10.1175/MWRD-20-0148.1.

}}, }}, J. M. Peters, and K. Friedrich, 2022: Environmental controls on simulated deep moist convection initiation occurring during RELAMPAGO-CACTI. J. Atmos. Sci., https://doi.org/10.1175/JAS-D-21-0226.1.

Nowotarski, C. J., J. M. Peters, and J. P. Mulholland, 2020: Evaluating the effective inflow layer of simulated supercell updrafts. J. Atmos. Sci., 148, 3507–3532, https://doi.org/10.1175/MWR-D20-0013.1.

Peters, J. M., 2016: The impact of effective buoyancy and dynamic pressure forcing on vertical velocities within two-dimensional updrafts. J. Atmos. Sci., 73, 4531–4551, https://doi.org/10.1175/JAS-D-16-0016.1.

}}, and D. R. Chavas, 2021: Evaluating the conservation of energy variables in simulations of deep moist convection. J. Atmos. Sci., 78, 3229–3246, https://doi.org/10.1175/JAS-D20-0351.1.

}}, W. M. Hannah, and H. Morrison, 2019a: The influence of vertical wind shear on moist thermals. J. Atmos. Sci., 76, 1645–1659, https://doi.org/10.1175/JAS-D-18-0296.1.

}}, C. Nowotarski, and H. Morrison, 2019b: The role of vertical wind shear in modulating maximum supercell updraft velocities. J. Atmos. Sci., 76, 3169–3189, https://doi.org/10.1175/JASD-19-0096.1.

}}, H. Morrison, W. M. Hannah, A. C. Varble, and S. E. Giangrande, 2020a: Thermal chains in ascending moist updrafts: Part II: Simulations. J. Atmos. Sci., 77, 3661–3681, https://doi.org/10.1175/JAS-D-19-0244.1.

}}, }}, C. J. Nowotarski, J. P. Mulholland, and R. L. Thompson, 2020b: A formula for the maximum vertical velocity in supercell updrafts. J. Atmos. Sci., 77, 3747–3757, https://doi.org/10.1175/ JAS-D-20-0103.1.

}}, C. J. Nowotarski, and G. L. Mullendore, 2020c: Are supercells resistant to entrainment because of their rotation? J. Atmos. Sci., 77, 1475–1495, https://doi.org/10.1175/JAS-D-19-0316.1.

}}, }}, and J. P. Mulholland, 2020d: The influences of effective inflow layer streamwise vorticity and storm-relative flow on supercell updraft properties. J. Atmos. Sci., 77, 3033–3057, https://doi.org/10.1175/JAS-D-19-0355.1.

}}, D. R. Chavas, and J. P. Mulholland, 2022a: Generalized lapse rate formulas for use in entraining CAPE calculations. J. Atmos. Sci., 79, 815–836, https://doi.org/10.1175/JAS-D-210118.1.

}}, H. Morrison, T. C. Nelson, J. N. Marquis, J. P. Mulholland, and C. J. Nowotarski, 2022b: The influence of shear on deep convection initiation. Part II: Simulations. J. Atmos. Sci., 79, 1691–1711, https://doi.org/10.1175/JAS-D-21-0144.1.

Romps, D. M., 2016: Reply to "Comments on 'MSE minus CAPE is the true conserved variable for an adiabatically lifted parcel.'" J. Atmos. Sci., 73, 2577–2583, https://doi.org/ 10.1175/JAS-D-15-0334.1.

}}, and A. B. Charn, 2015: Sticky thermals: Evidence for a dominant balance between buoyancy and drag in cloud updrafts. J. Atmos. Sci., 72, 2890–2901, https://doi.org/10.1175/ JAS-D-15-0042.1.

}}, and Z. Kuang, 2010a: Do undiluted convective plumes exist in the upper troposphere? J. Atmos. Sci., 67, 468–484, https://doi.org/10.1175/2009JAS3184.1.

}}, and }}, 2010b: Nature versus nurture in shallow convection. J. Atmos. Sci., 67, 1655–1666, https://doi.org/10.1175/ 2009JAS3307.1.

Rotunno, R., and J. B. Klemp, 1982: The influence of the shearinduced pressure gradient on thunderstorm motion. Mon. Wea. Rev., 110, 136–151, https://doi.org/10.1175/1520-0493(1982)110,0136:TIOTSI.2.0.CO;2.

Rousseau, R. R., D. J. Kirshbaum, and M. K. Yau, 2017: Initiation of deep convection over an idealized mesoscale convergence line. J. Atmos. Sci., 74, 835–853, https://doi.org/10.1175/JASD-16-0221.1.

Savre, J., and M. Herzog, 2019: A general description of entrainment in buoyant cloudy plumes including the effects of mixinginduced evaporation. J. Atmos. Sci., 76, 479–496, https://doi.org/10.1175/JAS-D-17-0326.1.

Schiro, K. A., F. Ahmed, S. E. Giangrande, and J. D. Neelin, 2018: GoAmazon2014/5 campaign points to deep-inflow approach to deep convection across scales. Proc. Natl. Acad. Sci. USA, 115, 4577–4582, https://doi.org/10.1073/pnas.1719842115.

Schlemmer, L., and C. Hohenegger, 2014: The formation of wider and deeper clouds as a result of cold-pool dynamics. J. Atmos. Sci., 71, 2842–2858, https://doi.org/10.1175/JAS-D-13-0170.1.

Scorer, R. S., 1957: Experiments on convection of isolated masses in buoyant fluid. J. Fluid Mech., 2, 583–594, https://doi.org/10.1017/S0022112057000397.

Sherwood, S. C., D. Hernandez-Deckers, and M. Colin, 2013: Slippery thermals and the cumulus entrainment paradox. J. Atmos. Sci., 70, 2426–2442, https://doi.org/10.1175/JAS-D-12-0220.1.

Simpson, J., and V. Wiggert, 1969: Models of precipitating cumulus towers. Mon. Wea. Rev., 97, 471–489, https://doi.org/10.1175/1520-0493(1969)097,0471:MOPCT.2.3.CO;2.

Thompson, R. L., C. M. Mead, and R. Edwards, 2007: Effective storm-relative helicity and bulk shear in supercell thunderstorm Environments. Wea. Forecasting, 22, 102–115, https://doi.org/10.1175/WAF969.1.

Torri, G., Z. Kuang, and Y. Tian, 2015: Mechanisms for convection triggering by cold pools. Geophys. Res. Lett., 42, 1943– 1950, https://doi.org/10.1002/2015GL063227.

Trapp, R. J., G. R. Marion, and S. W. Nesbitt, 2017: The regulation of tornado intensity by updraft width. J. Atmos. Sci., 74, 4199–4211, https://doi.org/10.1175/JAS-D-16-0331.1.

Turner, J. S., 1962: The starting plume in neutral surroundings. J. Fluid Mech., 13, 356–368, https://doi.org/10.1017/S0022112062000762.

}}, 1964: The dynamics of spherical masses of buoyant fluid. J. Fluid Mech., 31, 481–490, https://doi.org/10.1017/S0022112064000854.

}}, and G. I. Taylor, 1957: Buoyant vortex rings. Proc. Roy. Soc. London, A239, 61–75, https://doi.org/10.1098/rspa.1957.0022.

Waite, M. L., and B. Khouider, 2010: The deepening of tropical convection by congestus preconditioning. J. Atmos. Sci., 67, 2601–2615, https://doi.org/10.1175/2010JAS3357.1.

Warren, R. A., H. Richter, H. A. Ramsay, S. T. Siems, and M. J. Manton, 2017: Impact of variations in upper-level shear on simulated supercells. Mon. Wea. Rev., 145, 2659–2681, https://doi.org/10.1175/MWR-D-16-0412.1.

Weisman, M. L., and J. B. Klemp, 1982: The dependence of numerically simulated convective storms on vertical wind shear and buoyancy. Mon. Wea. Rev., 110, 504–520, https://doi.org/10.1175/1520-0493(1982)110,0504:TDONSC.2.0.CO;2.

Yang, G. Y., and J. M. Slingo, 2001: The diurnal cycle in the tropics. Mon. Wea. Rev., 129, 784–801, https://doi.org/10.1175/ 1520-0493(2001)129,0784:TDCITT.2.0.CO;2.

Zhao, M., and P. H. Austin, 2003: Episodic mixing and buoyancysorting representations of shallow convection: A diagnostic study. J. Atmos. Sci., 60, 892–912, https://doi.org/10.1175/15200469(2003)060,0892:EMABSR.2.0.CO;2.